The Astrophysical Journal, 971:169 (16pp), 2024 August 20 https://doi.org/10.3847/1538-4357/ad5e78

Environmental Effects on the Stellar Mass Function in a $z \sim 3.3$ Overdensity of Galaxies in the COSMOS Field*

Ben Forrest[1], Brian C. Lemaux[1,2], Ekta A. Shah[1], Priti Staab[1], Roy R. Gal[3], Lori M. Lubin[1], M. C. Cooper[4], Olga Cucciati[5], Denise Hung[2,3], Ian McConachie[6], Adam Muzzin[7], Gillian Wilson[8], Sandro Bardelli[5], Letizia P. Cassarà[9], Wenjun Chang[6], Finn Giddings[3], Emmet Golden-Marx[10], Nimish Hathi[11], Stephanie M. Urbano Stawinski[4], and Elena Zucca[5]

[1] Department of Physics and Astronomy, University of California Davis, One Shields Avenue, Davis, CA 95616, USA; bforrest@ucdavis.edu
[2] Gemini Observatory, NSF's NOIRLab, 670 N. A'ohoku Place, Hilo, HI 96720, USA
[3] University of Hawai'i, Institute for Astronomy, 2680 Woodlawn Drive, Honolulu, HI 96822, USA
[4] Department of Physics and Astronomy, University of California, Irvine, 4129 Frederick Reines Hall, Irvine, CA 92697, USA
[5] INAF Osservatorio di Astrofisica e Scienza dello Spazio di Bologna, Via Piero Gobetti 93/3, 40129 Bologna, Italy
[6] Department of Physics & Astronomy, University of California Riverside, 900 University Avenue, Riverside, CA 92521, USA
[7] Department of Physics and Astronomy, York University, 4700, Keele Street, Toronto, ONMJ3 1P3, Canada
[8] Department of Physics, University of California Merced, 5200 North Lake Road, Merced, CA 95343, USA
[9] INAF-IASF Milano, Via Alfonso Corti 12, 20133, Milano, Italy
[10] Department of Astronomy, Tsinghua University, Beijing 100084, People's Republic of China
[11] Space Telescope Science Institute, Baltimore, MD 21218, USA
Received 2024 February 23; revised 2024 June 4; accepted 2024 July 1; published 2024 August 16

Abstract

We present an analysis of the number density of galaxies as a function of stellar mass (i.e., the stellar mass function (SMF)) in the COSMOS field at $z \sim 3.3$, making a comparison between the SMF in overdense environments and the SMF in the coeval field. In particular, this region contains the Elentári proto-supercluster, a system of six extended overdensities spanning ∼70 cMpc on a side. A clear difference is seen in the high-mass slope of these SMFs, with overdense regions showing an increase in the ratio of high-mass galaxies to low-mass galaxies relative to the field, indicating a more rapid buildup of stellar mass in overdense environments. This result qualitatively agrees with analyses of clusters at $z \sim 1$, though the differences between protocluster and field SMFs at $z \sim 3.3$ are smaller. While this is consistent with overdensities enhancing the evolution of their member galaxies, potentially through increased merger rates, whether this enhancement begins in protocluster environments or even earlier in group environments is still unclear. Though the measured fractions of quiescent galaxies between the field and overdense environments do not vary significantly, implying that this stellar mass enhancement is ongoing and any starbursts triggered by merger activity have not yet quenched, we note that spectroscopic observations are biased toward star-forming populations, particularly for low-mass galaxies. If mergers are indeed responsible, high-resolution imaging of Elentári and similar structures at these early epochs should then reveal increased merger rates relative to the field. Larger samples of well-characterized overdensities are necessary to draw broader conclusions in these areas.

Unified Astronomy Thesaurus concepts: Galaxy evolution (594); High-redshift galaxy clusters (2007)

1. Introduction

The environment in which a galaxy resides plays an important role in its evolution. Obvious differences exist in the local Universe between the populations of galaxies in massive, evolved clusters and populations of galaxies in the field across a wide range of properties, including stellar mass, star formation rate (SFR), age, color, morphology, velocity dispersion, and metallicity (e.g., Dressler 1984; Kauffmann et al. 2004; Thomas et al. 2005). These differences are consistent with cluster galaxies having a faster and/or earlier evolutionary timescale than field galaxies and this signal is seen in the most overdense environments out past $z \gtrsim 1$ (e.g., Kawinwanichakij et al. 2017; Papovich et al. 2018; Mei et al. 2023). The strength of this signal begins to decrease or perhaps reverse by $z \gtrsim 1.5$ (Tran et al. 2010; Nantais et al. 2016; Pérez-Martínez et al. 2022; Edward et al. 2023; Taamoli et al. 2024), though some systems with elevated quenched fractions (QFs) do still appear at earlier epochs (e.g., Zavala et al. 2019; McConachie et al. 2022; Ito et al. 2023). In fact, at very early epochs, many galaxies in protoclusters, the progenitors of today's clusters, appear to have enhanced SFRs relative to the field (e.g., Capak et al. 2011; Hatch et al. 2011; Wang et al. 2016; Pérez-Martínez et al. 2023; Staab et al. 2024), suggesting that the effect of an overdense environment is to increase SFRs at early times. This may subsequently deplete the molecular gas content of these galaxies, as seen in low redshift galaxies (e.g., Fumagalli et al. 2009), thus inhibiting future star formation and leaving the galaxy more massive and with older stellar populations than galaxies that continue forming stars. This is consistent with findings of enhanced molecular gas reservoirs and gas fractions in clusters,

* Some of the data presented herein were obtained at Keck Observatory, which is a private 501(c)3 nonprofit organization operated as a scientific partnership among the California Institute of Technology, the University of California, and the National Aeronautics and Space Administration. The Observatory was made possible by the generous financial support of the W. M. Keck Foundation.

protoclusters, and groups relative to the field at high redshift (e.g., Noble et al. 2019; Shen et al. 2021a; Jin et al. 2021), a trend that also disappears around $z \sim 1.5$ (e.g., Alberts et al. 2022; Williams et al. 2022). However, the specific physical mechanisms responsible for any such environmental effects to take place and whether there is a particular density threshold or timescale required for these effects is unclear.

The combined effects of these processes can be seen by analyzing the number density of galaxies as a function of their stellar mass, which is an integral of the SFR of a galaxy across cosmic time. The shape of this stellar mass function (SMF) between nearby galaxies in clusters and in the field varies significantly, with galaxies in overdense regions showing a larger ratio of high-mass to low-mass galaxies (e.g., Blanton & Moustakas 2009). Some evidence suggests that this variation in shape may be entirely due to changes in shape and/or normalization of the SMF of red, early-type, quiescent populations, with the shape of the star-forming galaxy SMF staying relatively similar between field and cluster environments (e.g., Peng et al. 2010), though this is not universally found (e.g., Annunziatella et al. 2014, 2016).

Evidence is mixed as to whether or not this is the case in higher redshift overdensities. Field surveys at $z \sim 1$ have shown that the SMF varies with environmental density (Bundy et al. 2006; Cooper et al. 2010a; Papovich et al. 2018). Targeted spectroscopic observations of cluster environments at $z \sim 1$, such as those in the ORELSE (Lubin et al. 2009), GCLASS (Muzzin et al. 2012), and GOGREEN (Balogh et al. 2017, 2020) surveys, have found differences between cluster and field population SMFs as well. The results from GCLASS (van der Burg et al. 2013) and GOGREEN (van der Burg et al. 2020) suggest that these differences are due to changes in the relative fraction of quenched galaxies; however, the shapes of the quiescent SMFs in both overdensity and field are statistically the same, as are the shapes of the star-forming SMFs. However, results from ORELSE (Tomczak et al. 2017) instead show the evolution of shape in both the quiescent and star-forming SMFs with environmental overdensity. While narrowband imaging of Hα emitters in two protoclusters at $z = 2.16$ (Shimakawa et al. 2018b) and $z = 2.53$ (Shimakawa et al. 2018a) show differences in SMF shape relative to the field, a compilation of results at $z \gtrsim 2$ found a combined protocluster SMF with shape consistent with that of the field for star-forming galaxies, while the shape of quiescent galaxy SMFs between environments showed minor differences (Edward et al. 2023).

While SMF analyses of field populations $z > 3$ are numerous (e.g., Marchesini et al. 2009; Stefanon et al. 2015; Marsan et al. 2022; Weaver et al. 2023), similar analyses of overdense environments are lacking. This stems from the difficulty of identification and characterization of high-redshift overdensities, which is several-fold. Photometric identification of candidate overdensities at these epochs requires deep multiband imaging, in particular in the near-infrared, in order to identify stellar mass limited samples of faint galaxies, to infer the location of features such as the Balmer break, which aid in constraining photometric redshifts, and to cover the large projected sizes of these structures ($\sim$10–15 comoving Mpc, and in some cases larger; Muldrew et al. 2015; Chiang et al. 2017; Cucciati et al. 2018). The low-density contrast of these structures with the coeval field combined with significant photometric redshift uncertainties means that significant spectroscopic follow-up is also required to obtain precise galaxy redshifts, confirm these structures, and allow for accurate density mapping of the systems and their surroundings.

Similarly, simulations have had some success replicating QFs and SMFs in the Universe over a range of redshifts (Pillepich et al. 2018; De Lucia et al. 2024), though some disagreement in the SMF for high stellar mass galaxies at $z \gtrsim 2.5$ has been noted (e.g., Steinhardt et al. 2016; Sherman et al. 2020). Cluster SMFs can also be well replicated out to $z \sim 1.5$, though the QFs of satellite galaxies are often severely different from observations (e.g., Bahé et al. 2017; Kukstas et al. 2023). Some of this mismatch can be attributed to slightly different definitions of, e.g., star-forming versus quiescent galaxies (Donnari et al. 2021). Recent results from the GAEA models (De Lucia et al. 2024) appear to replicate the observed QF from GOGREEN clusters at $z \sim 1$ (van der Burg et al. 2020).

An assumption often made in attempting to understand the environmental effects on galaxy evolution is that the cluster satellite galaxies are drawn from the same population as the field, and have simply fallen into a massive halo that proceeds to influence member galaxies. Many works have also suggested that such influences begin even before infall into a massive cluster, in the earlier protocluster or group environments in what has been termed "preprocessing" (Balogh et al. 2000; Fujita 2004; De Lucia et al. 2012; Donnari et al. 2020). However, a recent analysis of the dark matter halos in simulations has suggested that the population of cluster galaxies may not in fact be drawn from the same parent population as field galaxies, which would allow for intrinsic halo properties to be responsible for observed population differences between field and cluster environments (Ahad et al. 2024).

Exploring whether there are environmental effects on the SMF in protocluster environments at $z > 3$ can lead to an increased understanding of the mechanisms in overdense environments that contribute to galaxy evolution. To that end, in this work, we build an SMF based on galaxies in the COSMOS field around the Elentári proto-supercluster at $z \sim 3.3$ (Forrest et al. 2023). To our knowledge, this is the first time such an analysis has been performed at this early epoch and is only possible due to a wealth of deep photometric and spectroscopic data as described in Section 2. We discuss the analysis methodology and results in Section 3 before presenting conclusions (Section 4). Throughout this work, we use the AB magnitude system (Oke & Gunn 1983) and assume a ΛCDM cosmology with $H_0 = 70$ km s^{-1} Mpc^{-1}, $\Omega_M = 0.3$, and $\Omega_\Lambda = 0.7$.

2. Data

2.1. Parent Photometric Catalogs

This work relies upon the considerable investment of observing time focused on the COSMOS field (Koekemoer et al. 2007; Scoville et al. 2007). The ultraviolet, optical, and near-infrared imaging in this field have been compiled most recently in the COSMOS2020 catalogs (Weaver et al. 2022), which contain over 1.5 million sources observed in up to 40 bandpasses over $\sim$1.5 deg^2. This includes space-based observations from GALEX (ultraviolet) (Zamojski et al. 2007), HST/ACS (optical) (Leauthaud et al. 2007), and Spitzer/IRAC (near-infrared) (Ashby et al. 2013, 2015, 2018; Steinhardt et al. 2014). Ground-based data includes ultraviolet CFHT/MegaCam

observations (Sawicki et al. 2019), optical data from Subaru/Suprime-Cam (Taniguchi et al. 2007, 2015) and Hyper Suprime-Cam (Aihara et al. 2019), and near-infrared observations from VISTA/VIRCAM (McCracken et al. 2012; Moneti et al. 2019).

The depth of the imaging involved in the construction of the COSMOS2020 catalogs as well as associated derived properties, including well-characterized photometric redshifts ($z_{\rm phot}$) and their probability distributions ($p(z)$), rest-frame colors, stellar masses, and SFRs are critical to this work. Unless otherwise stated, we use the COSMOS2020 Classic catalog, and the associated properties derived using `LePhare` (Arnouts et al. 1999; Ilbert et al. 2006). These characterizations use the same process as described in Ilbert et al. (2013), and include galaxy templates from Bruzual & Charlot (2003), Polletta et al. (2007), and Onodera et al. (2012), and stellar templates from Pickles (1998), with additional templates for white and brown dwarfs as well as active galactic nuclei. Allowed dust attenuation curves include Small Magellanic Cloud (Prevot et al. 1984), starburst (Calzetti et al. 2000), and starburst +2175Å profiles (Fitzpatrick & Massa 1986), and a Chabrier (2003) initial mass function is assumed.

2.2. Spectroscopy

2.2.1. Field Surveys

The COSMOS field has also been the target of many spectroscopic surveys, several of which are included in this work. The VIMOS Ultra-Deep Survey (VUDS; Le Fèvre et al. 2015), targeted $\sim 10^4$ objects across the COSMOS, ECDFS, and VVDS-2h fields with the VIMOS instrument on ESO-Very Large Telescope (VLT; Le Fèvre et al. 2003). This survey preferentially selected targets for follow-up that had $z_{\rm phot} \gtrsim 2$ and were deep enough to reliably detect continuum for $i \sim 25$ objects.

The zCOSMOS survey (Lilly et al. 2007) also used the VIMOS spectrograph on the VLT and consisted of two subsamples. The zCOSMOS-bright subsample targeted $\sim 2 \times 10^4$ galaxies with $I < 22.5$ and thus mainly confirmed galaxies across $0.1 < z < 1.2$ over the entire COSMOS ACS field. The zCOSMOS-deep subsample targeted $\sim 10^4$ galaxies in the central portion of the field believed to have $1.4 < z < 3.0$ based on their colors (K. Daichi et al. 2024, in preparation).

The DEIMOS 10k Spectroscopic Survey (Hasinger et al. 2018) similarly targeted $\sim 10^4$ objects, using the DEIMOS instrument on the Keck II telescope (Faber et al. 2003). While the entirety of this survey was in the COSMOS field, there was no photometric redshift cut applied, and thus, the majority of objects with spectroscopic redshifts are at $z < 2$. Sample selection was heterogeneous, with several subsamples of galaxies, including (among others) Spitzer/MIPS sources, high-redshift candidates, and optical counterparts of X-ray sources.

These surveys have also used similar spectroscopic redshift quality flagging systems. The base flag for each object is one of the following: 0—no redshift measured, 1—low confidence redshifts, 2, 3, 4, 9—secure redshifts (estimated $\gtrsim$75% reliability; Lilly et al. 2007; Le Fèvre et al. 2013; Cassata et al. 2015). Each flag may also prepended with a number X, indicating that the target either has broad lines observed in the spectrum ($X = 1$), the target is a serendipitous detection ($X = 2$), or the target is a serendipitous detection at the location of the target (i.e., chance alignment or merger; $X = 3$).

2.2.2. Targeted Surveys—Charting Cluster Construction with VUDS and ORELSE

The Charting Cluster Construction with VUDS (Le Fèvre et al. 2015) and ORELSE (Lubin et al. 2009) (C3VO) survey (Lemaux et al. 2022) has used the Keck/DEIMOS and Keck/MOSFIRE (McLean et al. 2010, 2012) instruments on the Keck telescopes to follow up candidate overdensities identified in density maps constructed from a combination of spectroscopic and photometric data across the CFHTLS-D1, ECDFS, and COSMOS fields (see Sections 3.1 and 3.2 for a description of these maps and candidate overdensity identification). The survey has observed ∼2000 galaxies across the three fields, approximately half with MOSFIRE and half with DEIMOS. Targeted regions included Hyperion ($z = 2.45$; Casey et al. 2015; Cucciati et al. 2018), PCl J1000+0200 ($z = 2.90$; Cucciati et al. 2014), PCl J0227-0421 ($z = 3.31$; Lemaux et al. 2014; Shen et al. 2021b), Elentári ($z = 3.33$; McConachie et al. 2022; Forrest et al. 2023), Smruti ($z = 3.47$; Forrest et al. 2017; Shah et al. 2024), and Taralay ($z = 4.57$; Lemaux et al. 2018; Staab et al. 2024).

All C3VO COSMOS observations used in this work are shown in Tables 1 and 2. MOSFIRE masks targeting Hyperion as well as the first three masks targeting Elentári used photometric redshifts and magnitudes from the COSMOS2015 catalog (Laigle et al. 2016) for target selection. Subsequent masks targeting Elentári (observed in 2023) selected objects based on $p(z)$, stellar masses, and rest-frame colors from the COSMOS2020 Classic catalog. DEIMOS masks prioritized targeting star-forming galaxies down to $i_{\rm AB} < 25.3$ with photometric redshifts near that of the overdensity in question, as detailed in Lemaux et al. (2022).

In this work, we focus on density maps constructed from data including VUDS and zCOSMOS spectroscopy, photometry from COSMOS2015 and COSMOS2020, and C3VO spectroscopic data taken prior to fall 2021 (the 2021B semester). Spectroscopic redshifts from other masks listed in Tables 1 and 2 are incorporated into subsequent pieces of the analysis, and are important for confirming redshifts of objects whose membership in Elentári is inconclusive from $p(z)$ alone.

2.2.3. Targeted Surveys—Massive Ancient Galaxies at z > 3 Near-infrared Survey

The Massive Ancient Galaxies at $z > 3$ Near-infrared Survey (MAGAZ3NE; Forrest et al. 2020) has used Keck/MOSFIRE to spectroscopically follow up ultramassive galaxies (UMGs; $\log(M_*/M_\odot) > 11$ at $z > 3$) and investigate their environments. It has thus far targeted ∼1000 galaxies across the UltraVISTA (COSMOS), VIDEO-XMM, and VIDEO-CDFS fields. This survey selected targets in the COSMOS field for follow-up based on observed galaxy spectral energy distributions (SEDs), $p(z)$, stellar masses, and SFRs from the UltraVISTA DR1 and DR3 catalogs (Muzzin et al. 2013a, A. Muzzin 2024, private communication).

This paper focuses on a set of six structures (S1–S6) at $z \sim 3.3$ named Elentári (Forrest et al. 2023). While it is unlikely that all six will collapse into a single system at $z = 0$, there are multiple pairs of structures that may do so. This system as a whole has over 100 spectroscopically confirmed members, and the best-characterized structure (S1) has an estimated $z = 0$ mass of 1.3×10^{14} $M_\odot$. Two of these (S1, S4) were spectroscopically confirmed via MAGAZ3NE spectroscopy

Table 1
C3VO Keck/MOSFIRE Observations in COSMOS

Target (z)	Mask	Bandpass	Date(s) Observed	Total Exp.Time (m)	Avg. Seeing (arcsec)
Hyperion (2.45)	Hyperion1	*H*	2020.03.09	150	0.71
	Hyperion2	*H*	2020.03.09	112	0.69
	Hyperion3	*H*	2020.03.10	106	0.66
	Hyperion4	*H*	2020.03.11	104	0.55
	Hyperion5	*H*	2020.03.11	106	0.55
	Hyperion6	*H*	2020.11.30	118	0.79
	Hyperion7	*H*	2020.11.30	164	0.86
			2021.01.06		
			2021.12.25		
Elentàri (3.33)	DONGOCps23n24_1	*K*	2021.12.26	102	0.77
	DONGOCps23n24_2	*K*	2021.12.26	102	0.68
	DONGOCps23n24_3	*K*	2022.10.15	48	0.86
	NEb_1	*K*	2023.02.03	90	0.86
	NEc_1	*K*	2023.03.30	60	0.67
	NEd_1	*K*	2023.03.30	42	0.81
	Bridge1	*K*	2023.02.03	84	0.89
			2023.03.30		
	Bridge2	*K*	2023.03.31	72	0.70
	SWa_1	*K*	2023.02.03	84	1.00
			2023.03.30		
	SWc_1	*K*	2023.03.31	48	0.93

Note. *H*-band exposures were 120 s each, and *K*-band exposures were 180 s each. The slit width was $0\farcs7$.

Table 2
C3VO Keck/DEIMOS Observations in COSMOS

Target (z)	Mask	Filter	Central Wavelength (Å)	Date(s) Observed	Total Exp.Time (m)	Avg. Seeing (arcsec)
Taralay (4.57)	dongN1C	GG400	6500	2017.12.26	210	0.8
	dongS1B	GG400	6500	2016.12.22	275	0.8
	dongD1	GG455	7200	2017.12.26	320	0.94
				2019.02.05		
				2019.12.24		
				2020.12.23		
	dongD2	GG455	7200	2020.02.02	360	0.78
				2020.12.10		
				2022.12.23		
	dongA1	GG455	7200	2021.01.17	299	0.84
				2022.01.10		
	dongA2	GG455	7200	2022.01.10	240	0.59
				2022.01.10		
PCl J1000+0200 (2.90)	dongC2D1	GG400	6500	2022.01.11	145	0.82
	dongC2N1	GG400	6500	2020.02.02	309	1.15
	dongC2S1	GG400	6500	2019.02.25	268	0.97
				2020.12.10		
				2020.12.23		
				2021.01.17		

Note. The 600ZD grating (600 lines/mm) was used for all observations.

(McConachie et al. 2022) as they contain UMGs, and the larger region was independently identified and then spectroscopically followed up with C3VO.

2.2.4. Spectroscopic Data Reduction

Details on the data reduction process and redshift assignment for zCOSMOS (Lilly et al. 2007), VUDS (Le Fèvre et al. 2015), and DEIMOS 10k (Hasinger et al. 2018) data can be found in the publications of those surveys. However, all surveys used a combination of automated initial redshift assignment followed by visual inspection and checking of results.

We reduced the C3VO MOSFIRE spectra using the MOSDEF 2D data reduction pipeline (Kriek et al. 2015). This pipeline was also used to re-reduce the MAGAZ3NE MOSFIRE data, which were initially reduced using the Keck-supported MOSFIRE Data Reduction Pipeline (DRP; version

2018). The MOSDEF pipeline subtracts the sky background noise, masks both cosmic rays and bad pixels, and rectifies each frame. It also identifies the trace of a star on a science slit, which is used to measure atmospheric seeing and throughput, as well as to account for any drift in telescope pointing by shifting individual frames to match the location of the star spectrum, which is particularly important when targeting the same mask for long periods without realigning due to flexure of the system (Hutchison et al. 2020). The program weights each exposure according to the seeing and throughput values before coadding the frames and applying a telluric correction and flux calibration. Combined with the weighting of individual frames, this method returns 2D spectra with increases in the signal-to-noise ratio (S/N) of ∼5% relative to the MOSFIRE DRP. The resultant 2D spectrum was collapsed in a narrow range around either the strongest emission line or along the entire wavelength axis for continuum sources. This was fit with a Gaussian, which was subsequently used for weighting the 1D spectral extraction (optimal extraction; Horne 1986).

A modified version of the `spec2D` pipeline (Cooper et al. 2012) was used to reduce C3VO-DEIMOS spectra. This program performs wavelength fitting, background sky subtraction, and 1D spectral extraction. Additional modifications are detailed in Lemaux et al. (2019) and include improvements in interpolation over the DEIMOS chip gap, throughput correction, and wavelength solution.

2.2.5. Spectroscopic Redshift Determination

The MOSFIRE spectra were visually inspected to identify galaxies with emission lines. At the redshifts considered in this work, emission lines from Hβ and the [O III]$\lambda\lambda$4959, 5007 doublet are the most obvious features, and when seen, a model consisting of three Gaussians is used to obtain a spectroscopic redshift. This model has four parameters—the redshift, the amplitudes of Hβ and [O III]λ5007, and the width of the lines. The level of stellar continuum is assumed to be constant over the spectral range of the observations, and is taken to be the weighted average flux outside of regions with emission lines. The amplitude of [O III]λ4959 is fixed to 30% that of [O III] λ5007 (e.g., Schreiber et al. 2018b). In this work, we are not concerned with the quantification of line velocity widths, velocity offsets, or any broad line components beyond obtaining a redshift as pertains to MOSFIRE spectra. A small number of galaxies at lower redshifts, which had Hα, [N II] $\lambda\lambda$6548, 6584, and [S II]$\lambda\lambda$6718, 6733 in the wavelengths probed by the MOSFIRE observations, were fit with a similar multi-Gaussian model. Each spectroscopic observation is additionally given a quality flag in the style of the zCOSMOS, VUDS, and DEIMOS 10k surveys described above, which denotes the confidence in the assigned spectroscopic redshift (see, e.g., Le Fèvre et al. 2015; Lemaux et al. 2022, for more details). Additionally, emission spatially offset from targeted galaxies that serendipitously fell in MOSFIRE slits (or in DEIMOS slits, see below) was re-extracted and the same redshift measurement and quality assessment process was performed on such detections.

The DEIMOS spectra were interactively assigned spectroscopic redshifts by using a modified version of the `zspec` environment (Newman et al. 2013) as described in Lemaux et al. (2022). The modified version of the `zspec` software incorporates empirical high-redshift galaxy templates from the VUDS and VVDS (Le Fèvre et al. 2004, 2013) surveys as well as high-resolution empirical Lyα templates from Lemaux et al. (2009). The quality flagging for these data follows a DEEP2 style flag (Newman et al. 2013). Similar to the VUDS flagging system, flags 3 and 4 represent high-confidence redshifts (>95% accuracy). For example, the observation of a single emission line skewed redward indicative of Lyα would result in flag 3, and the observation of multiple spectral features would result in flag 4. Flags 1 and 2 indicate low confidence redshifts. For consistency with the MOSFIRE data and redshifts from the field surveys, C3VO-DEIMOS objects with a quality flag of 2 are changed to a quality flag of 1 when creating the master spectroscopic catalog (next section). All spectra were independently inspected and flagged by two of the authors (E.S. and B.C.L.) and any objects receiving disparate redshifts/flags were reconciled via a reinspection of the spectra and associated photometry (when available).

2.3. Catalog Matching and Remodeling SEDs

While target selection for the various spectroscopic surveys used in this work came from different parent photometric catalogs, we compare the spectroscopic redshifts, sky coordinates, and *i*- and *K*-band magnitudes from the spectroscopic survey catalogs to the photometric redshifts, coordinates, and magnitudes in the same bandpasses from the COSMOS2020 Classic photometric catalog to find the best match. For galaxies targeted in multiple surveys, only the highest quality flag entry was kept. See Appendix A for more details regarding the matching process. Of the 40008 final combined spectroscopic catalog entries, 37771 (94.4%) have a match in the COSMOS2020 Classic catalog. Additionally, 26676 (66.7%) spectroscopic targets have moderate-high quality spectroscopic redshift measurements $0 < z < 7$ (quality flags X2, X3, X4, or X9).

With confirmed redshifts of these galaxies, it is necessary to remodel their physical properties, which will change from those given in COSMOS2020 unless the photometric redshift is identical to the spectroscopic redshift. While there are many programs used to model galaxy SEDs, in this work, we use `LePhare` (Arnouts et al. 1999; Ilbert et al. 2006), as this program is used in the COSMOS2020 catalogs. We remodel all spectroscopically confirmed galaxies using the same setup as in COSMOS2020 with the redshift now fixed to the spectroscopic redshift. Detailed descriptions of these choices can be found in the catalog publications above, as well as in Ilbert et al. (2009).

As will be described shortly, we also perform a Monte Carlo (MC) resampling of the $p(z)$ for all galaxies without a high-confidence spectroscopic redshift. For each such galaxy, we run `LePhare` with the redshift fixed to values from $3.0 < z < 3.7$ (the redshift range considered in this work) with $\Delta z = 0.05$. The results from this grid are then interpolated to the redshift of a galaxy determined in an individual MC iteration. We found that the differences in the fit stellar mass and SFR between adjacent redshift runs for a given galaxy differ by >0.1 dex in less than 0.3% and 2.3% of cases, respectively, more than sufficient for the studies herein, which validates this interpolation.

3. Analysis

3.1. Voronoi Tesselation Monte Carlo Mapping

We use the Voronoi tesselation Monte Carlo (VMC) mapping technique to determine galaxy environmental density,

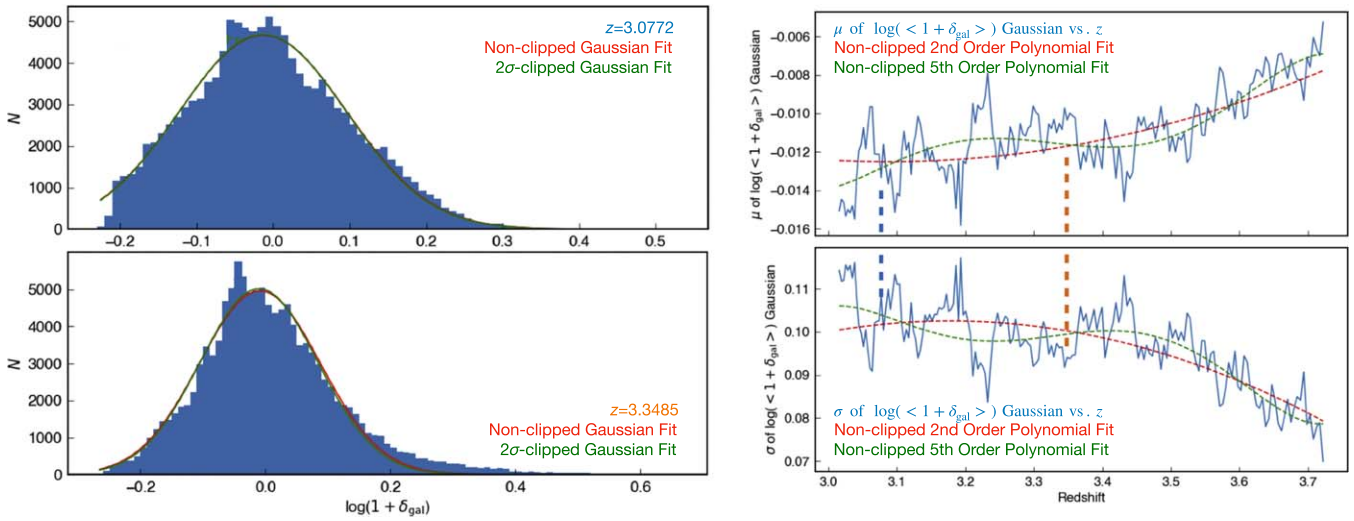

Figure 1. The process for determining the spread in voxel overdensity values for a given redshift slice. Left: histograms of all voxel overdensity values (median set equal to zero) in redshift slices of $z = 3.0772$ (top) and $z = 3.3485$ (bottom). A Gaussian model is fit to the distribution at each slice, which produces a fit mean (μ) and standard deviation (σ). Right: the plot of the fit μ (top) and σ (bottom) values for each slice of the VMC map considered in this work. A polynomial is then fit to this distribution to smooth out the effects of any large-scale structures on these values, and these polynomial values are used to determine the overdensity significance (σ_δ) of a given voxel. Herein, we use the value of a fifth-order polynomial (green), though using a second-order polynomial (red), for example, does not affect the results. The redshifts of the two slices shown on the left are given by dashed vertical lines.

a method that has been extensively tested and used to find overdense structures previously (Lemaux et al. 2017, 2018, 2022; Tomczak et al. 2017; Cucciati et al. 2018; Hung et al. 2020; Shen et al. 2021b; Forrest et al. 2023). This method uses a combination of spectroscopic redshifts and photometric redshift probability distributions to statistically determine density in three-dimensional space.

3.1.1. Density Maps

Voronoi cells are generated by drawing boundaries that are equidistant from the two nearest galaxies in projected space. This strategy cannot be effectively extended to the redshift dimension due to the redshift uncertainties of objects in photometric catalogs as well as the uncertain contributions of peculiar velocities for spectroscopically confirmed galaxies. While high spectroscopic completeness could minimize the effects of the former, the spectroscopy in this work is too sparse to do so. As a result of these uncertainties along the line of sight, the volume of interest is divided into redshift slices and only galaxies within such a slice are considered. The slice width is determined from a combination of photometric redshift uncertainties and a consideration of overdensity sizes. Structures can be missed either if slices are too narrow—when associated galaxies are not grouped together—or if slices are excessively wide, which results in a decrease in overdensity signal. Similar to previous work, slices of 7.5 pMpc in depth are used ($\delta z \sim 0.036$ at $z = 3.35$) with an oversampling factor of 10×; that is, the distance between central redshifts in adjacent slices is 0.75 pMpc.

We perform 100 MC iterations, in which the $p(z)$ of every photometric galaxy is resampled to minimize the effect of photometric redshift uncertainties. A statistical treatment of spectroscopic redshifts is also included, in which the quality flag of the spectroscopic redshift determines how often the spectral redshift is used as compared to a draw from that galaxy's $p(z)$ (see Appendix B of Lemaux et al. 2022). In practice, the spectroscopically targeted galaxies with redshift quality flags of 3 or 4 have their spectroscopic redshift used in ∼99.4% of all iterations (high confidence), galaxies with redshift quality flags 2 or 9 have their spectroscopic redshift used in ∼70.0% of all iterations, and galaxies with redshift quality flags 0 or 1 do not have their spectroscopic redshifts used at all. In such iterations where the spectroscopic redshift is not used, the redshift of a galaxy for that iteration is determined via a draw from the galaxy's $p(z)$.

For each of the 100 iterations, Voronoi tesselation is performed on all objects with magnitude $[3.6] < 24.8$ that fall into a given redshift slice for a given iteration. The results for each iteration are then regridded onto a regular grid of size 75×75 pkpc, with the median density at a grid point in all iterations assigned to each voxel, $\Sigma_{\mathrm{VMC},\alpha,\delta,z}$. Figure 3 of Tomczak et al. (2017) provides a visualization of this process.

3.1.2. Overdensity Maps

The typical density of the Universe evolves with time, and the measurement of the average density from the VMC method is subject to differences in data quality, detection bands, magnitude cuts, etc. As a result we are more concerned with the relative overdensity of a galaxy's environment rather than a pure density value. This overdensity value is calculated by normalizing each density in a redshift slice by the median density of all voxels in the map at the same redshift, $\log(1 + \delta_{\mathrm{VMC},\alpha,\delta,z}) = \log(1+\Sigma_{\mathrm{VMC},\alpha,\delta,z}/\ \tilde{\Sigma}_{\mathrm{VMC},z})$. Additionally, given the extended nature of high-redshift protoclusters, the possibility exists that the entire field may be over- or underdense in a particular redshift slice, which could bias our overdensity calculations. To account for this, we fit a Gaussian to the distribution of $\log(1 + \delta_{\mathrm{VMC},\alpha,\delta,z})$ values in each redshift slice, to obtain the average and standard deviation of the overdensity values therein (left panels of Figure 1). A fifth-order polynomial is then fit to the average overdensities as a function of redshift, removing any effects of field filling over- or underdensities and obtaining a smoothed overdensity distribution, $\log(1 + \delta_{f^5,\alpha,\delta,z})$ (right panels of Figure 1). We note that the differences between these two measures of overdensity, $\log(1 + \delta_{\mathrm{VMC},\alpha,\delta,z})$ and $\log(1 + \delta_{f^5,\alpha,\delta,z})$, are on

the order of several parts in 1000, which is $\sim 10\times$ smaller than the spread of values at a given redshift, and thus in general does not have a significant effect on our results.

Finally, the overdensity of a galaxy $\log(1+\delta_{\rm gal})$ is simply the fit overdensity value $\log(1+\delta_{f^5,\alpha,\delta,z})$ of the voxel, which contains the galaxy's three-dimensional position in space in a given iteration. We also calculate the number of standard deviations of a galaxy's overdensity value, σ_δ, above or below the fit median using the fit standard deviation value at the redshift of interest. This value will be the primary overdensity metric used in this work.

3.2. Structure Identification

As described in Cucciati et al. (2018) and Shen et al. (2021b), we identify overdense structures by finding all contiguous voxels with $\sigma_\delta > 2$ (>5 for peak regions). The volume enclosed within these envelopes can then be converted to a total mass based on the average comoving matter density, average overdensity of voxels within the envelope, and the galaxy sampling bias. Following this process, a set of coeval structures with enclosed masses $\log(M_{\rm tot}/M_\odot) \gtrsim 14$ in close proximity at $3.20 < z < 3.45$ were identified in Forrest et al. (2023). While that work focused on characterization of the structures themselves, in this work, we analyze the galaxy populations therein.

In many studies of overdense structures, members are defined as being within some spherical radius of a central point in the structure. However, at early epochs such as this, protocluster systems are not necessarily spherically symmetric in nature, and the VMC maps allow for accounting and inclusion of some of these asymmetries. This lack of symmetry also means that an accurate determination of the extent and overdensity of these structures is critical to drawing accurate conclusions about the effects such environments have on their component galaxies.

3.2.1. Effects of Uneven Spectroscopic Sampling

To this end, analyzing the dependence of overdensity significance on spectroscopic completeness is a critical test. Using the above VMC method, a real overdensity with all members spectroscopically confirmed will have a stronger signal (higher σ_δ) than the same overdensity with no spectroscopically confirmed members, as the latter will have the total signal spread out in redshift space due to the width of the $p(z)$ for member galaxies. Alternatively, if a region has little to no spectroscopically confirmed galaxies, it is possible that the VMC data may identify an overdensity when none is truly there. Such a situation occurs when the $p(z)$ distributions of many galaxies in a small projected area, potentially including background and foreground objects, overlap significantly in redshift space.

We attempt to quantify these effects by considering galaxies with $[3.6] < 24.8$ and analyzing the spatial variance of (1) the spectroscopic sampling rate (SSR)—the number of galaxies photometrically within a given volume that has been spectroscopically targeted divided by the total number of galaxies with a photometric redshift within that same volume, and (2) the spectroscopic redshift fraction (SzF), which we define here as the number of galaxies that have a high confidence spectroscopic redshift within some volume divided by the number of galaxies with a photometric redshift within that same volume. We calculate these fractions in spatial bins of $3' \times 3'$ over the full $3.0 < z < 3.7$ redshift range considered for Elentári and the associated field. This is shown in Figure 2, along with the number of objects with photometric redshifts in each bin.

As can be seen in the bottom two panels of Figure 2, the SSR and spectroscopic redshift fraction (SzF) both fall off significantly outside of the VUDS footprint (dashed line), while the number of photometric targets stays roughly constant across the same boundary (top panel). Overdensities identified in regions with low SzF have an increased probability of being false detections as the signal may be dominated by broad photometric redshift probability distributions, e.g., S6 from Forrest et al. (2023), shown by the very extended gray contour in the northeast. However, some regions with low SzF may still be real if there are significant spectroscopic confirmations, e.g., the extension of S1 from Forrest et al. (2023) (red contours) outside of the VUDS footprint. This particular region has 14 confirmed spectroscopic members from targeted follow-up with MAGAZ3NE (McConachie et al. 2022). Clearly, further spectroscopic observations of potential overdensities in such regions can resolve this issue.

The possibility also exists that overdensities identified in regions with high SzF and SSR, while real, are less overdense in reality than the VMC maps would suggest. To ensure this effect is not influencing our results significantly, we rerun the VMC mapping analysis ignoring the spectroscopic redshifts from C3VO and MAGAZ3NE. Removing this spectroscopy from our sample limits the effects of intentional spectroscopic targeting of overdense regions, as all other surveys targeted galaxies across the COSMOS field as a whole. Rerunning the VMC mapping and overdensity detection in this manner produces the results shown in Figure 3, where new structure overdensity contours of $+2\sigma$ and $+5\sigma$ are shown as filled cyan and magenta regions, respectively, and the original Elentári overdensities as reported in Forrest et al. (2023) are shown as open colored contours.

Using the same structure identification routine, the centers of commonly identified structures differ by medians of 78″ (0.58 pMpc) in projection and 0.002 in redshift. However, this can be split into those structures mostly within the VUDS footprint (S2—orange contour on Figure 3—and S3 in green) with projected offsets of 8.″1 (0.06 pMpc) and 22″ (0.16 pMpc), and those that extend outside (S1 in red and S6 in gray) with projected offsets of 133″ (0.99 pMpc) and 160″ (1.2 pMpc). For the former two structures the two maps result in volume differences of 8.0% and 0.7% and mass differences of 0.04 dex and 0.01 dex, in remarkable agreement. The overdensity-weighted central three-dimensional locations for commonly identified $+5\sigma$ peaks differ in the two cases by similar amounts, with median differences of 18″ (0.13 pMpc) in projection and 0.002 in redshift. Noting that the typical systematic uncertainty for determining the stellar mass of a galaxy at similar epochs is estimated to be $\sim$0.2 dex (Mobasher et al. 2015; Leja et al. 2019), the characterization of these structures' masses and positions is robust to the effects of targeted spectroscopic follow-up at the levels obtained. Regions extending beyond the VUDS outline without significant additional spectroscopy may be difficult to characterize accurately without additional data, however. On the whole, we conclude that the targeted spectroscopic follow-up has not significantly biased our characterization of the Elentári system,

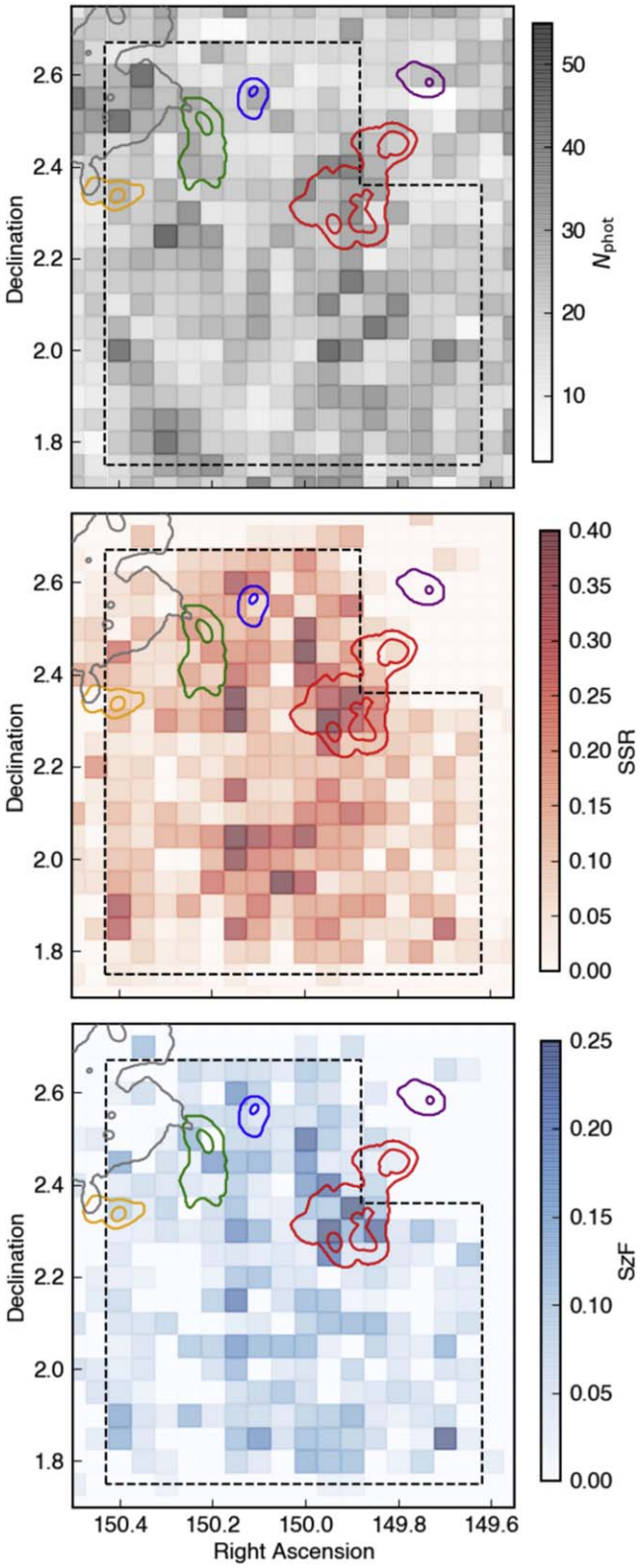

Figure 2. The relative numbers of photometric and spectroscopic galaxies in COSMOS in $3' \times 3'$ bins across $3.0 < z < 3.7$ near the VUDS footprint (black dashed outline). Top: the number of galaxies from the COSMOS2020 catalog in $3' \times 3'$ bins with photometric redshifts $3.0 < z < 3.7$. The structures associated with Elentári (Forrest et al. 2023) are shown as contours representing 2σ and 5σ overdensities collapsed over $3.0 < z < 3.7$. Middle: similar to the top panel, but showing the SSR. Bottom: similar to the top panel, but showing the SzF.

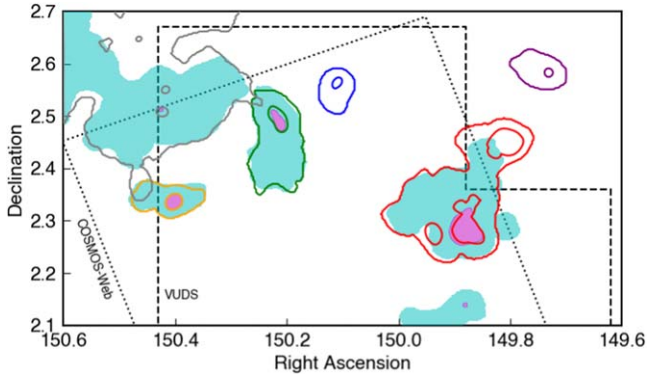

Figure 3. The recovery of overdensities in the field of interest with targeted follow-up spectroscopy (empty colored contours at $+2\sigma$ and $+5\sigma$) and without targeted follow-up spectroscopy (filled cyan and magenta contours at $+2\sigma$ and $+5\sigma$). The former set is as presented in Forrest et al. (2023).

and for the remainder of this work, consider the structure extends as in Forrest et al. (2023).

3.3. The SMF

In order to investigate environmental effects on galaxy evolution, we construct SMFs based on the overdensities derived from the VMC maps. Similar to the generation of the VMC maps, we run 100 realizations drawing from the $p(z)$ of galaxies without reliable spectroscopic redshifts and determine the significance of the overdensity in which each galaxy resides, σ_δ, from the VMC map at the galaxy's redshift in the realization. All galaxies are subsequently refit using `LePhare` with the same methodology as when refitting the spectroscopically confirmed galaxies, but instead using the redshifts drawn from the $p(z)$ and the interpolated fits with $\delta z = 0.05$. The resultant galaxy stellar masses are then used to construct SMFs. The volume associated with an SMF is the volume of the VMC map within the associated redshift and σ_δ cuts.

For each realization, SMFs are constructed over $3.20 < z < 3.45$ from galaxies in bins of σ_δ: $-5 < \sigma_\delta < 2$ (field), $2 < \sigma_\delta < 3$, $3 < \sigma_\delta < 4$, and $\sigma_\delta > 4$. There are insufficient galaxies at $\sigma_\delta > 5$ to recover an SMF in this regime with a large enough S/N to make significant conclusions. Similarly, considering only galaxies within each structure of Elentári separately leads to small numbers of high-mass galaxies, which makes the uncertainties too large to justify drawing strong conclusions. Consistent results are found from constructing a combined SMF for all galaxies in all regions of Elentári and from calculating the SMF based on overdensity values of $\log(1 + \delta_{gal})$ as well. We confirm that the field SMF is insensitive to other possible definitions, for example averaging galaxies with $-5 < \sigma_\delta < 2$ at $3.0 < z < 3.2$ and $3.5 < z < 3.7$ and that the field SMF is also in very good agreement with those over $3 < z_{phot} < 4$ based on the COSMOS2015 (Davidzon et al. 2017) and COSMOS2020 (Weaver et al. 2023) catalogs.

The median SMFs in each overdensity bin from all realizations are shown in Figure 4, with error bars representing the 16th–84th percentile range. In addition to the vertical offset that is a result of the selected regions being overdense, a difference in the shape of the SMFs is also apparent and can be seen in Figure 5, in which the ratio of each SMF with that of the field is displayed. In all overdense regions, there is a trend of increasingly elevated SMF relative to the field with

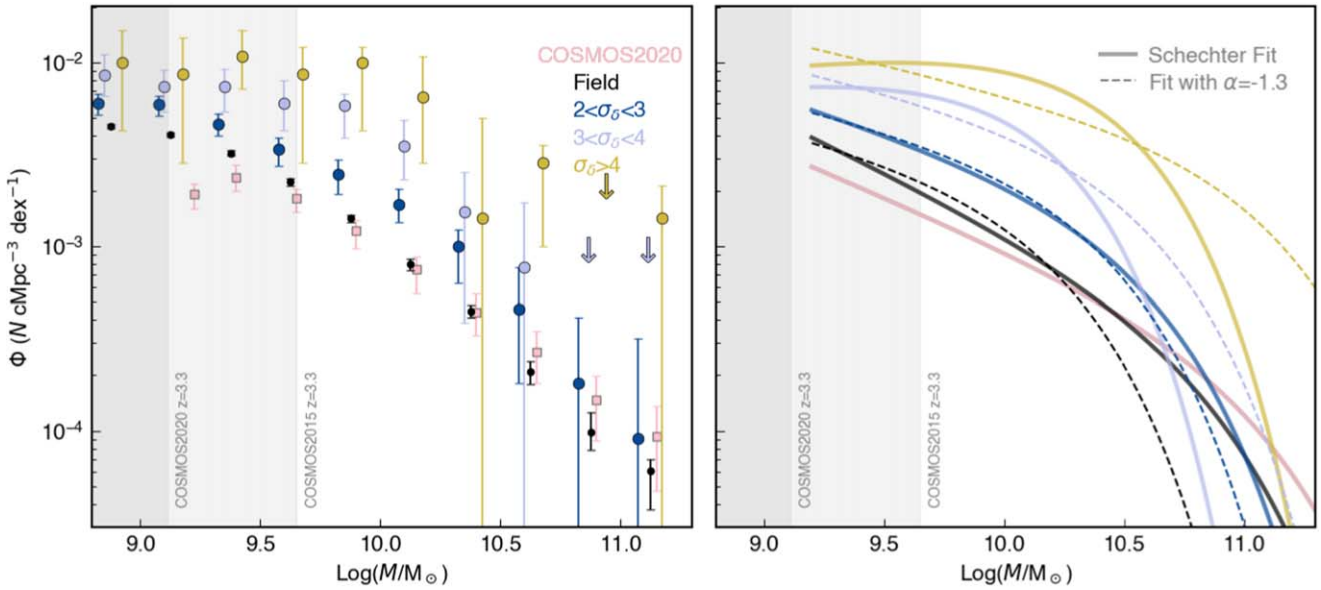

Figure 4. The SMF in several bins of overdensity at $3.20 < z < 3.45$. Left: the SMF of the field from COSMOS2020 over $3.0 < z < 3.5$ (Weaver et al. 2023) is shown as a series of pink-filled squares, while the field as measured in this work is shown as a series of black points. The SMFs of galaxies in bins of $2 < \sigma_\delta < 3$, $3 < \sigma_\delta < 4$, and $\sigma_\delta > 4$ are shown as blue, periwinkle, and gold points, respectively. Error bars from this work represent the range of 16th to 84th percentiles from MC iterations added in quadrature to Poisson noise. Note that this does not include uncertainty due to cosmic variance, which is the dominant source of error in the COSMOS2020 analysis, and thus the error bars between the two works should not be compared. Masses below the stellar mass completeness limits at $z = 3.3$ for the COSMOS2015 and COSMOS2020 catalogs are shaded. Right: the best-fit Schechter function to each measured SMF is shown as a solid line with the same color scheme. Another fit to each SMF performed fixing $\alpha = -1.3$ is shown as a dashed curve.

increasing stellar mass, a pattern also seen in lower redshift cluster SMFs (Tomczak et al. 2017; van der Burg et al. 2020), as well as in individual protoclusters at $z = 2.16$ (Shimakawa et al. 2018b) and $z = 2.53$ (Shimakawa et al. 2018a). This higher ratio of high-mass to low-mass galaxies in overdense regions is consistent with galaxies in protocluster environments undergoing, or having previously undergone, increased stellar mass buildup relative to field galaxies.

We compare our results to those from the $z \sim 1$ ORELSE survey (Tomczak et al. 2017), which used a similar methodology for the determination of overdensity. The qualitative trends seen in the $z \sim 1$ cluster sample are similar to those in this work, with the ratio of high-mass to low-mass galaxies increasing with increasing overdensity. Additionally, as shown in Figure 5, when converting our SMFs from σ_δ to $\log(1 + \delta_{\rm gal})$ we find that the SMF for galaxies at similar overdensities appears the same at both $z \sim 1$ and $z \sim 3.3$. The field of interest in this work and those in Tomczak et al. (2017) have different photometric bandpasses and depths, as well as different spectroscopic depths and SSR/SzF, which add uncertainty to such a direct comparison. However, this similarity of SMFs at similar overdensities at different redshifts would be consistent with the hypothesis that group environments, galaxy associations with lower total masses ($\sim 10^{13}$ $M_\odot$) than protoclusters, are host to evolutionary effects (e.g., mergers) that "preprocess" galaxies before their eventual residence in cluster environments (Zabludoff et al. 1996; McGee et al. 2009; De Lucia et al. 2012; Bahé et al. 2019; Reeves et al. 2021).

Additionally, we fit a single-Schechter function (Schechter 1976) to each SMF, first allowing the characteristic turnover mass (M^*), faint-end slope (α), and normalization (ϕ^*) parameters to vary, and then again fixing $\alpha = -1.3$, in rough agreement with previous results (e.g., Marchesini et al. 2009; Muzzin et al. 2013b; Tomczak et al. 2014). The best-fit parameterizations are given in Table 3. We compare the

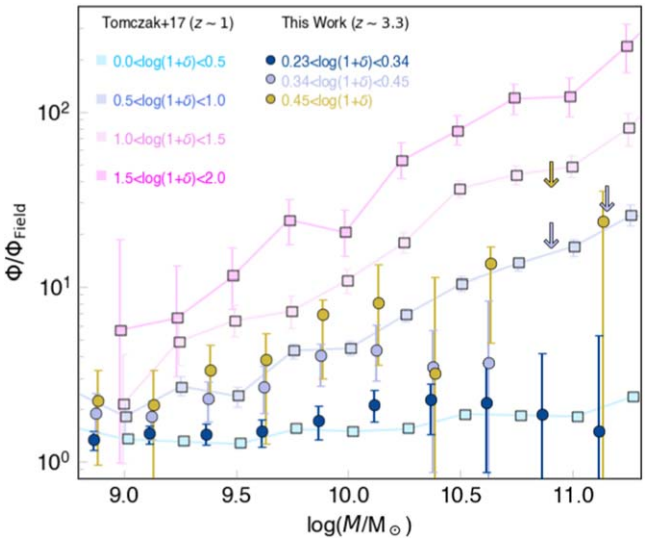

Figure 5. The ratio of the stellar mass function at different overdensities to that observed in the field. The gold, periwinkle, and blue points are as in Figure 4 and represent galaxies in regions with overdensities of roughly $0.23 < \log(1 + \delta) < 0.34$, $0.34 < \log(1 + \delta) < 0.45$, and $\log(1 + \delta) > 0.45$ at $z \sim 3.3$. Similar points from Tomczak et al. (2017) at $z \sim 1$ are shown as squares for comparison. SMFs of similar overdensity seem to scale to the field in similar manners at both redshifts.

characteristic turnover mass and faint-end slope values to those from studies of $z \sim 1$ cluster SMFs (Tomczak et al. 2017; van der Burg et al. 2020) shown in Figure 6. In general, we find that M^* decreases and α becomes shallower with increasing overdensity. This is perhaps not so much due to the stellar mass of the average galaxy decreasing, but is instead a result of environmental processes increasing the number of galaxies around or just below the characteristic mass. This increase may be due to increased merger rates in overdense environments

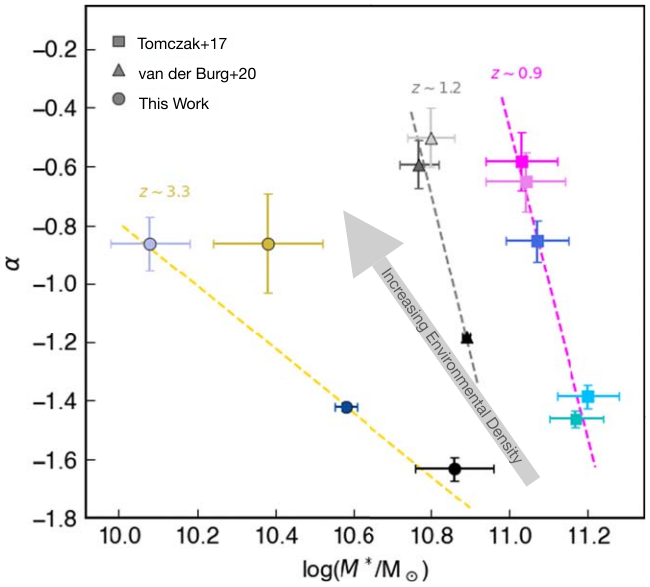

Figure 6. Comparison of the characteristic mass (M^*) and faint-end slope (α) fit values from studies of the SMF in overdense environments. Values from this work are shown as filled circles of the same colors as in Figure 4, values from $z \sim 1.2$ GOGREEN clusters van der Burg et al. (2020) are grayscale triangles, and values from $z \sim 0.9$ ORELSE clusters Tomczak et al. (2017) are cyan to magenta-filled squares. A simple weighted linear fit for each data set is shown in gold, gray, and magenta, respectively.

Table 3
The Parameters of the Schechter Function Fits to the SMFs at Varying Densities

Density Bin	$\log(M^*/M_\odot)$	α	$\phi^*/(10^{-3}\mathrm{Mpc}^{-3})$
$\sigma_\delta < 2$	10.86 ± 0.10	-1.63 ± 0.04	0.16 ± 0.04
	10.20 ± 0.05	$= -1.3$	0.87 ± 0.07
$2 < \sigma_\delta < 3$	10.58 ± 0.03	-1.42 ± 0.01	0.66 ± 0.04
	10.40 ± 0.03	$= -1.3$	1.07 ± 0.05
$3 < \sigma_\delta < 4$	10.08 ± 0.10	-0.86 ± 0.09	4.83 ± 0.78
	10.58 ± 0.19	$= -1.3$	1.49 ± 0.33
$\sigma_\delta > 4$	10.38 ± 0.14	-0.86 ± 0.17	6.57 ± 2.00
	11.10 ± 0.20	$= -1.3$	1.40 ± 0.35

Note. The best-fit values for varying M^*, α, and ϕ^* are shown as are the results for fixing $\alpha = -1.3$.

(Tomczak et al. 2017), preferential enhancement of SFR in high-mass galaxies in overdense environments, increased numbers of quiescent galaxies (Nantais et al. 2016; van der Burg et al. 2018, 2020), or an underlying bias in galaxies in overdense environments relative to those in the field (Ahad et al. 2024).

Finally, we confirm that the observed difference in SMF shape is not due to preferential scattering of low-mass galaxies with broader $p(z)$ out of the overdensity. We use a toy model to resample redshifts, stellar masses, and overdensity membership of 1000 galaxies 1000 times in a mock region of sky, and then reconstruct SMFs (details in Appendix B). No evidence for a mass-dependent bias is observed.

3.4. Quiescent Fractions

The fraction of galaxies with SFRs below the main sequence of star formation (i.e., quenched) at a given epoch is significantly increased in cluster environments relative to the coeval field out to $z \gtrsim 1$ (van der Burg et al. 2013; Tomczak et al. 2017; van der Burg et al. 2020), though the majority of massive satellite galaxies at this epoch appear to have been quenched before cluster infall (Baxter et al. 2022; Werner et al. 2022). High-redshift protocluster environments at $z \gtrsim 2$ do not generally show these same quiescent fractions, but some counterexamples appear to exist, at least with regard to high-mass galaxies (Chartab et al. 2020; Shi et al. 2021; Ito et al. 2023), which has been seen in one of the peaks of Elentári (McConachie et al. 2022). Analyzing how the SMFs of such quenched galaxies vary relative to the field environments can help uncover the mechanisms responsible for the accelerated evolution of galaxies in overdense systems (e.g., Tomczak et al. 2017; Papovich et al. 2018).

Table 4
The Number of Star-forming (N_{SF}) and Quiescent Galaxies (N_Q) and the Associated QFs in the Field and Overdensity Samples across $3.20 < z < 3.45$ Identified Using *UVJ* Colors and the SFMS

	$UVJ_{\mathrm{M>9.1}}$	$UVJ_{\mathrm{M>10}}$	$\mathrm{SFMS}_{\mathrm{M>9.1}}$	$\mathrm{SFMS}_{\mathrm{M>10}}$
$N_{\mathrm{SF,field}}$	3593^{+129}_{-137}	$463.0^{+37.0}_{-38.0}$	3688^{+131}_{-136}	$477.0^{+39.0}_{-36.0}$
$N_{\mathrm{Q,field}}$	$130.0^{+40.0}_{-29.0}$	$50.0^{+23.0}_{-14.0}$	$37.0^{+17.0}_{-12.0}$	$37.0^{+15.0}_{-12.0}$
$N_{\mathrm{SF,od}}$	$398.0^{+81.0}_{-71.1}$	$61.5^{+24.0}_{-22.1}$	$398.0^{+88.6}_{-65.1}$	$59.0^{+29.0}_{-18.9}$
$N_{\mathrm{Q,od}}$	$7.5^{+13.8}_{-7.1}$	$4.0^{+6.3}_{-4.0}$	$2.0^{+5.4}_{-1.7}$	$2.0^{+5.4}_{-1.7}$
QF_{field}	$3.49^{+1.07}_{-0.78}$	$9.75^{+4.48}_{-2.73}$	$0.99^{+0.46}_{-0.32}$	$7.20^{+2.92}_{-2.33}$
QF_{od}	$1.85^{+3.40}_{-1.74}$	$6.11^{+9.66}_{-6.11}$	$0.50^{+1.34}_{-0.43}$	$3.28^{+8.77}_{-2.84}$

Note. Two sets of results are shown, one only considering galaxies with masses $\log(M_*/M_\odot) > 10.0$ and one considering galaxies with masses $\log(M_*/M_\odot) > 9.1$.

For each of the 100 $p(z)$ sampling realizations, we calculate the number of quiescent and star-forming galaxies over $3.20 < z < 3.45$ in two ways. First, we use the popular comparison of $(U-V)$ and $(V-J)$ rest-frame colors (e.g., Williams et al. 2009; Muzzin et al. 2013a; Straatman et al. 2016) as modeled by `LePhare` and the wedge location specified for $2.0 < z < 3.5$ from Whitaker et al. (2011). We also fit the relation between SFR and stellar mass (e.g., Daddi et al. 2007; Noeske et al. 2007; Salmon et al. 2015) by finding the median SFR in overlapping bins of width 0.2 dex with centers separated by 0.01 dex, smoothing via a first-order Savitzsky–Golay filter, and fitting with a quadratic polynomial. Galaxies with SFRs more than 1 dex below this "star-forming main sequence" (SFMS) are then considered quiescent. The resultant numbers of galaxies with $\log(M_*/M_\odot) > 9.1$, the mass completeness of the COSMOS2020 Classic catalog at this redshift, are given in Table 4.

While the numbers of identified quiescent galaxies in the overdense regions are too small to construct SMFs from, we can compute quiescent fractions, which we plot in the right panel of Figure 7, along with quiescent/star-forming selections for an example MC iteration in the left and middle panels. No statistically significant differences between field and overdense environments are seen, though the uncertainties are significant. The two methodologies also seem to be in general agreement, with the *UVJ* color selection identifying more quiescent galaxies than the SFMS cut, particularly for galaxies with $\log(M_*/M_\odot) < 10$.

We do note, however, that while the COSMOS2020 photometric catalog is complete down to $\log(M_*/M_\odot) \sim 9.1$ at $z \sim 3.3$, most of the spectroscopy used for the construction of the VMC maps is biased toward the detection of star-forming

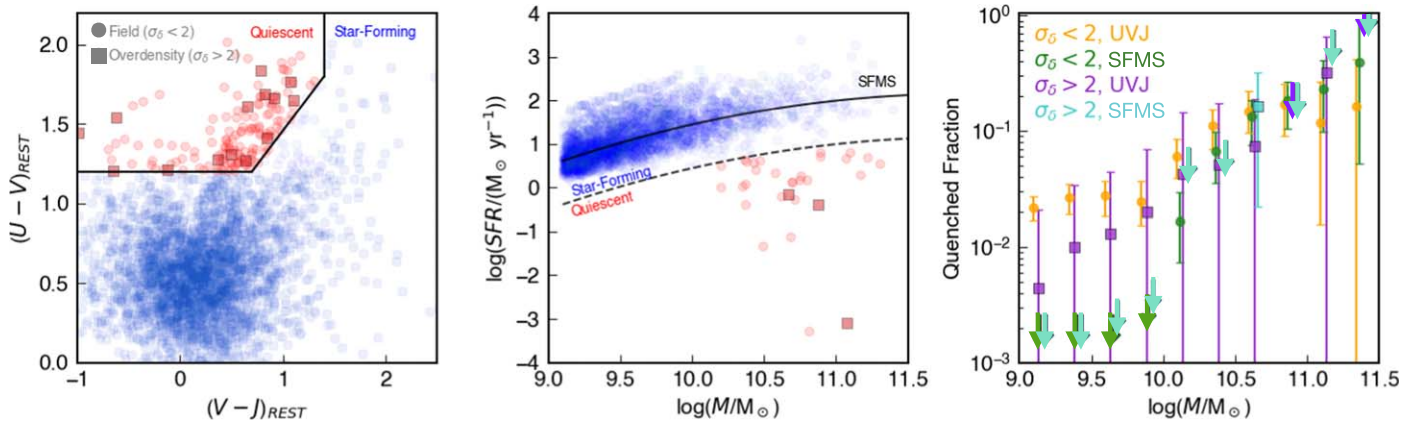

Figure 7. The identification of star-forming and quiescent galaxies at $3.20 < z < 3.45$. Left: the rest-frame *UVJ* color–color plane for a single MC iteration. Red symbols above/left of the dividing wedge are considered quiescent, with squares indicating those galaxies in overdense environments and filled circles indicating galaxies in the field. Blue symbols below/right of the dividing wedge are classified as star forming. Center: the SFR–stellar mass plane for a single MC iteration. The solid black curve is the median relation termed the SFMS, while the dashed curve is 1 dex below the SFMS and is used to distinguish between star-forming and quiescent galaxies. The symbol colors and shapes remain the same. Right: the QF as a function of stellar mass averaged over all 100 MC iterations. Orange-filled circles represent the field QF identified using the *UVJ* selection. Green-filled circles represent the field QF identified using the SFMS selection. Purple-filled squares represent the overdensity QF identified using the *UVJ* selection. Turquoise-filled squares represent the overdensity QF identified using the SFMS selection. Downward-facing arrows indicate upper limits. While an increasing trend with stellar mass is seen, the sample sizes are insufficient to distinguish between the QFs in field and overdense environments.

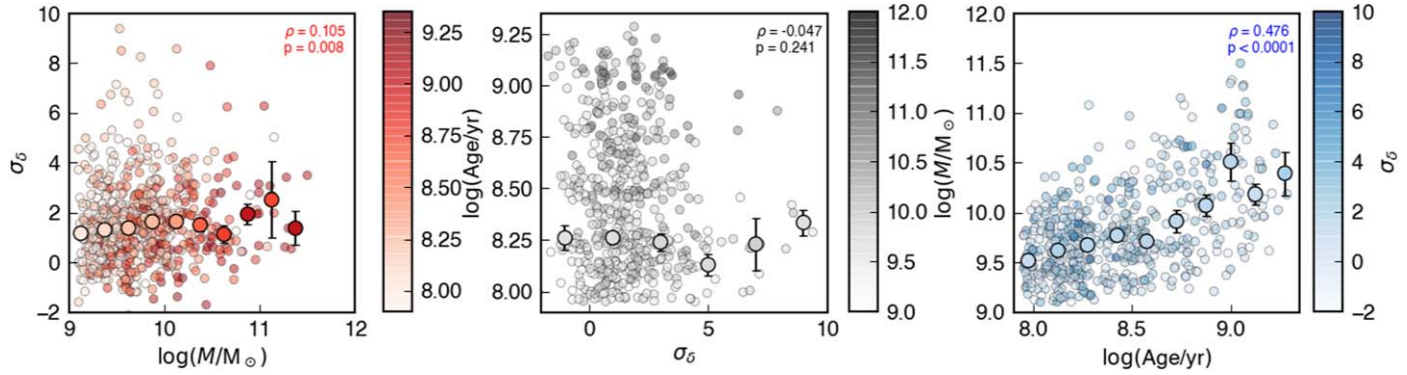

Figure 8. Comparison of stellar mass, stellar age, and environmental overdensity from SED fitting for spectroscopically confirmed galaxies at $3.0 < z < 3.7$ in COSMOS shown in three different projections. Median values are shown by the large circles, with the error bars representing the uncertainty on the calculated median. The Spearman ρ coefficient and p-value are shown in each panel for the set of parameters on the ordinate and abscissa.

galaxies, which may artificially decrease the QFs seen here. The follow-up observations with MOSFIRE are less sensitive to this bias, but still no enhancement in QF relative to the field is seen in the overdense environments, which were targeted with MOSFIRE.

3.5. Relations between Stellar Mass, Age, and Overdensity

Observed increases in the masses of galaxies residing in overdense environments relative to the field population could be caused by factors such as enhanced SFRs due to gas inflows or bursts of star formation as a result of increased merger rates. Depending on when these effects occur, it is possible that the ages of galaxies of a given mass will have a dependence upon their environment as seen at lower redshifts (e.g., Cooper et al. 2010b), though these appear small at $z \sim 1.3$ (Webb et al. 2020). While in theory, stellar ages can be discerned from spectral absorption features and the shape of the SED, the spectra of the vast majority of sources in this work do not have the requisite S/N to measure ages precisely, having spectral detections of emission lines only. In an attempt to discern age differences between the field and structure populations, we fit the photometry of each spectroscopically confirmed galaxy with the redshift fixed to the spectroscopic redshift using the `LePhare` (Arnouts et al. 1999; Ilbert et al. 2006) and FAST++ (Schreiber et al. 2018a) programs. We then compare the stellar mass and age derived from these fits to the σ_δ of each galaxy and perform a Spearman correlation test (Figure 8).

As seen in the SMF analysis, we find a weak ($\rho = 0.105$), though significant ($p = 0.008$) correlation between massive galaxies and overdense environments, similar to that found over $2 < z < 5$ in Lemaux et al. (2022). A commonly found correlation between stellar mass and age is also recovered ($\rho = 0.476$, $p < 0.0001$). However, there is no significant trend for this sample between age and overdensity. This could indicate that gas-rich mergers that trigger bursts of star formation are not responsible for the increased stellar masses of galaxies in these overdense environments, although some studies suggest that such bursts are not as pronounced at higher redshifts (Shah et al. 2022). In this case, mergers could build high stellar mass galaxies without adding a significantly younger stellar population. Some other intrinsic differences

between galaxies in overdense and field environments may also be responsible (Ahad et al. 2024). It should be noted though that age determinations from SED fitting have significant uncertainties as well as degeneracies with stellar mass and dust extinction (e.g., Mobasher et al. 2015), and thus, drawing strong conclusions from these tests is not supported.

4. Conclusions

In this work, we construct and compare SMFs and quiescent fractions in several bins of environmental overdensity in the COSMOS field centered on the Elentári overdensity at $z \sim 3.33$. Such an analysis is only possible at these epochs with the extensive amounts of photometry and spectroscopy available in well-studied fields such as COSMOS. These are used to build a three-dimensional density map to accurately estimate the environmental density field in which a galaxy resides. We consider in this work galaxies above the approximate stellar mass completeness of the COSMOS2020 catalog at $z \sim 3.3$, $\log(M_*/M_\odot) \sim 9.1$.

We observe distinct shapes of the SMF between galaxies in overdense environments and galaxies in the field at $3.20 < z < 3.45$, with the densest regions having number densities $\sim 6\times$ that of the field for galaxies with $\log(M_*/M_\odot) \sim 10.0$, compared to only $\sim 3\times$ that of the field for galaxies with $\log(M_*/M_\odot) \sim 9.5$. This distinction clearly indicates that the environment in which a galaxy resides begins to have an effect on its evolution prior to the galaxy entering a cluster environment. The increased number of high-mass galaxies in dense environments is suggestive of the long-theorized "preprocessing," in which the masses of such galaxies are enhanced in protocluster or even group systems via mergers and/or increased in situ SFRs before infall into proper clusters, eventually resulting in the quenching of star formation in these overdense systems before quenching in field galaxies. The quiescent fractions of galaxies in field and overdense environments do not differ, peaking at ~20%–30% for galaxies with $\log(M_*/M_\odot) \sim 11.0$. This may suggest that while processes of mass enhancement in overdense environments have begun, processes, which enhance the QF in these same environments have not yet had significant effects. We note, however, that the uncertainties on these measurements are large and that the spectroscopic surveys in this work are in general more sensitive to star-forming populations. More dedicated observations of quiescent candidates identified from photometry are required for stronger conclusions.

Finally, we compare the relationship between stellar mass, stellar age, and environmental overdensity of spectroscopically confirmed galaxies. We find statistically significant positive correlations between stellar mass and stellar age, as well as between stellar mass and environmental overdensity. This again suggests that the overdense structure of the Elentári proto-supercluster may be affecting the evolution of member galaxies through enhanced stellar mass growth, but is inconclusive on the matter of enhanced quenching of member galaxies. Further observations, particularly of the densest protocluster cores in Elentári are necessary to uncovering the extent and significance of these effects.

Acknowledgments

The authors wish to recognize and acknowledge the very significant cultural role and reverence that the summit of Maunakea has always had within the indigenous Hawaiian community. We are most fortunate to have the opportunity to conduct observations from this mountain. This work is also based on observations collected at the European Southern Observatory under ESO programs 175.A-0839, 179.A-2005, and 185.A-0791, as well as work supported by the National Science Foundation under grant No. 1908422. G.W. gratefully acknowledges support from the National Science Foundation through grant AST-2205189 and from HST program number GO-16300.

This work has relied heavily upon code developed by other people, for which we are quite thankful.

Software: Astropy (Robitaille et al. 2013; Price-Whelan et al. 2018; The Astropy Collaboration et al. 2022), FAST++ (Schreiber et al. 2018a), IPython (Pérez & Granger 2007), LePhare (Arnouts et al. 1999; Ilbert et al. 2006), Matplotlib (Hunter 2007), NumPy (Oliphant 2007).

Appendix A
Object Matching

We use observations of galaxies from the zCOSMOS (Lilly et al. 2007), VUDS (Le Fèvre et al. 2015), and DEIMOS 10k (Hasinger et al. 2018) spectroscopic surveys, as well as observations taken with Keck/MOSFIRE as part of the C3VO (Lemaux et al. 2022) and MAGAZ3NE (Forrest et al. 2020) surveys to construct a master spectroscopic catalog. The targets in these samples are drawn from various observational catalogs in the COSMOS field and here we detail the process of matching these observations to galaxies in the COSMOS2020 photometric catalog (Weaver et al. 2022).

A.1. Astrometric Correction

For each spectroscopic survey, each spectroscopic entry (s_i) is matched to the nearest photometric catalog member (p_{j0}) in the projected space. The coordinates for spectroscopic entries are then updated based on the median positional offsets between the data sets, median ($\Delta\alpha_{i,j0}$) and median ($\Delta\delta_{i,j0}$), providing a first-order astrometric correction. These median offsets are $\lesssim 0\farcs1$ in all cases.

A.2. Positional Threshold

Catalog matching is performed again to find the nearest photometric catalog member (p_j). We then use the distribution of distances between matches to calculate our matching tolerance, considering that this distribution is composed of a combination of correct matches and random nearest matches in cases where the spectroscopic target is not in the photometric catalog. These two components become clear by analyzing the histogram of logarithmic distance separations (Figure A1).

We fit a Gaussian to each of these distributions and take the 3σ upper limit for the main peak (assumed to be correct matches) to be the distance threshold within which to search for a given spectroscopic survey. Alternatively, taking the 3σ limit from fitting a single Gaussian to the entire distribution or by choosing the distance at which the contributions of the two Gaussians are equal while changing the number of galaxies matched does not result in differences to the scientific conclusions of this work. For objects in the VUDS, C3VO, zCOSMOS, and DEIMOS 10k surveys, this search radius threshold is $0\farcs70$, $0\farcs53$, $0\farcs49$, and $1\farcs35$, respectively, which

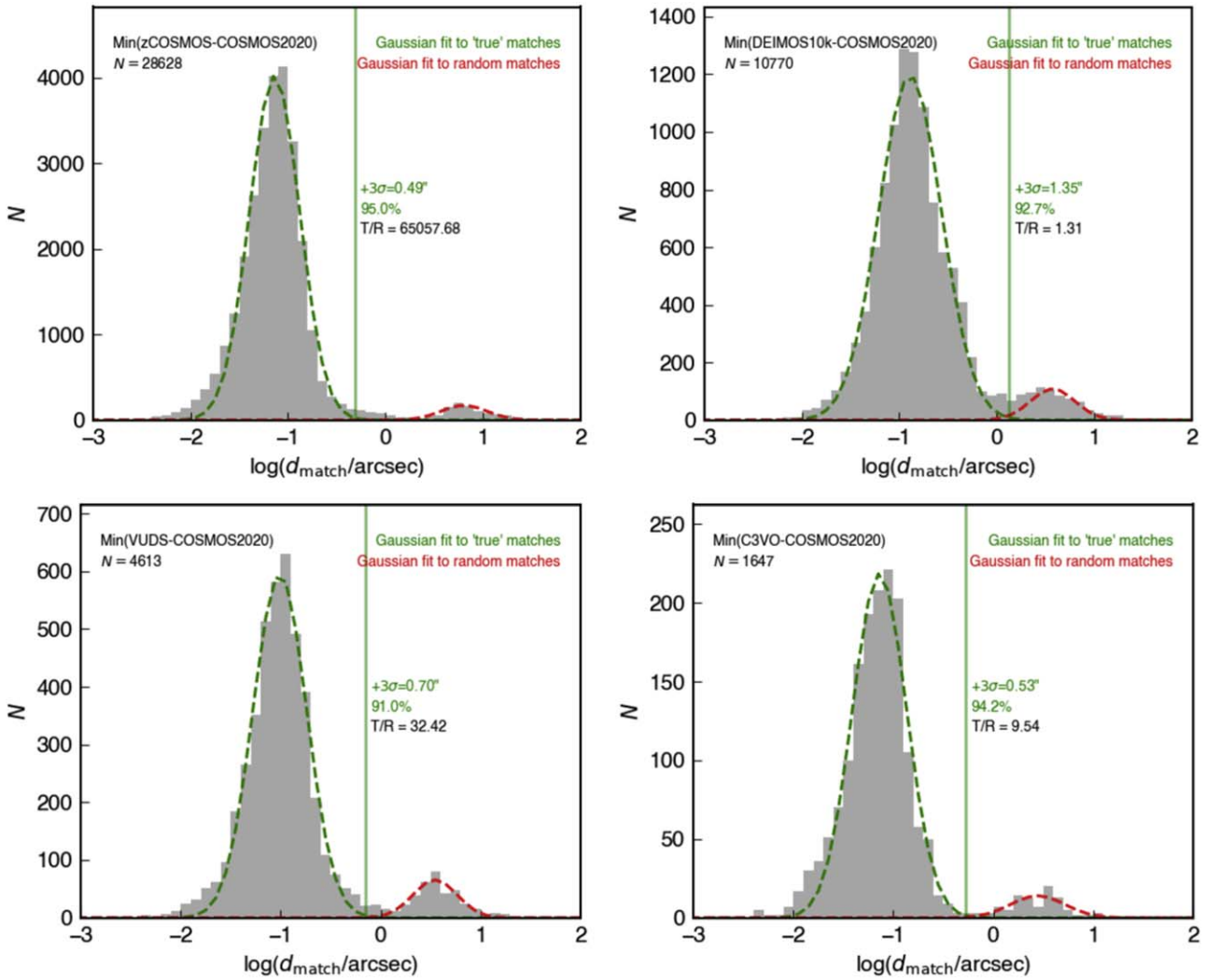

Figure A1. Determination of matching thresholds. The distribution of distances from each spectroscopic object to the nearest photometric catalog member after a bulk astrometric correction is plotted as a gray histogram. A two Gaussian model is fit, with the green representing "true" matches and the red representing random matches. A green vertical line shows the $+3\sigma$ value of the "true" Gaussian fit, with the associated separation, the percentage of matches within that separation, and the ratio of the amplitude of the two Gaussian components at that distance given.

successfully matches 91.0%, 94.2%, 95.0%, and 92.7% of entries.

A.3. Single Matches

If there is a single photometric match to a spectroscopic object within the 3σ radius threshold of a survey, we take the two entries to be matches to the same object.

A.4. Multiple Matches

Many of the spectroscopic entries in the catalog have more than one photometric catalog member, which satisfies both the distance and magnitude threshold cuts above. In these cases, comparisons are also made between the spectroscopic redshift and the photometric redshifts of potential matches, as well as differences in their total *i*- and *K*-band magnitudes, resulting in a four-parameter comparison. If no other spectroscopically confirmed galaxies are nearby, the photometric member with the better-weighted combination of values is determined to be the correct match. If another spectroscopic entry is also nearby, the photometric and spectroscopic entries are paired based on the closest positional match.

A.5. No Matches

There are 2237 spectroscopic entries in the catalog that have no photometric catalog members that satisfy the distance threshold cuts above. These objects are retained in the final spectroscopic catalog and are not considered when generating the VMC maps or further analyses as they do not have the requisite photometry for performing SED fitting to determine stellar mass, SFR, etc.

A.6. Duplicates

At this point, each spectroscopic object is considered to be matched to the correct photometric catalog object. As such, photometric catalog objects with multiple spectroscopic matches exist and are given a true multi-spec flag. If these spectroscopic entries (which have a quality flag of 3, 4, or 9) have the same redshift, this is considered the spectroscopic redshift. When discrepant spectroscopic redshifts with identical good quality flags exist, the instrument and survey are used to determine the correct redshift. In order of priority, these are C3VO, MAGAZ3NE, VUDS, DEIMOS 10k, zCOSMOS (updated catalog), and zCOSMOS (original catalog).

Appendix B
SMF Significance Testing

It is possible that the observed difference in the SMF of members of the Elentári protostructure and the coeval field could be partially or entirely due to differential effects related to large photometric redshift uncertainties. More specifically, assuming that lower-mass galaxies have broader $p(z)$, they are more likely to scatter in and out of different environmental bins than high-mass galaxies. If both the field and overdensity SMF have the same intrinsic shape and are simply different in normalization, then due to the fairly small redshift extent of the higher-density bins presented in this work, a broader $p(z)$ for lower-mass galaxies relative to their more massive counterparts would potentially lead to a differential loss of such galaxies within the highest density bins as they will scatter out of the volumes associated with the higher-density environments and into those associated with the lower density environments more frequently than higher mass galaxies. Under such a scenario, the SMF in higher-density bins would then appear to have a lower ratio of low-mass to high-mass galaxies than the field.

We use a toy model to test whether such an effect can reproduce the observed results. We start by assuming that the only difference in the field and overdensity SMFs is the normalization (factor of 10 difference) and that overdensities have a volume filling factor of ∼3% (Chiang et al. 2017), and then populate a mock region of sky with 1000 galaxies. The probability of a random galaxy residing in the field/overdensity will then be

$$p_f = \frac{0.97 \times 1}{0.03 \times 10 + 0.97 \times 1} \times 100\% = 76.4\%, \quad \text{(B1)}$$

$$p_o = \frac{0.03 \times 10}{0.03 \times 10 + 0.97 \times 1} \times 100\% = 23.6\%. \quad \text{(B2)}$$

Field galaxies are distributed randomly across the mock projected area and assigned a random redshift in the range $3.0 < z < 3.7$. Overdensity members are assigned positions based on a random draw from a Gaussian in each dimension such that the $\pm 2\sigma$ values encompass 3% of the total volume. The centers and widths of these Gaussians are $\mu_\alpha = \mu_\delta = 0$, $\mu_z = 3.325$, $\sigma_\alpha = \sigma_\delta = 0.14$, and $\sigma_z = 0.0625$. Each galaxy is then assigned a stellar mass drawing from the SMF.

With each galaxy assigned a "true" position, redshift, and stellar mass, we now assign redshift probability distributions based on uncertainties from the COSMOS2020 catalog. Each galaxy is assigned a $p(z)$, which is an asymmetrical Gaussian. The center of this Gaussian is drawn from a Gaussian characterized by the mean and standard deviation of the offset between spectroscopic and photometric redshifts at $3.0 < z < 3.7$ (0.09 ± 0.29). Similarly, the width of each side of the Gaussian is drawn from a Gaussian characterized by the mean and standard deviation of the 16th and 84th percentiles of the $p(z)$ of galaxies at similar stellar mass at $3.0 < z < 3.7$.

We then run 1000 MC iterations, in each one randomly drawing a "measured" redshift from the $p(z)$ of each galaxy. A measured stellar mass is determined from the difference between measured and "true" redshifts combined with an uncertainty of 0.2 dex (e.g., Mobasher et al. 2015; Wang et al. 2024). The overdensity or field membership of a galaxy is then determined based on the three-dimensional position of the galaxy relative to the known overdensity extent. An SMF is then constructed for the field and the overdense regions using the medians of all 1000 iterations with uncertainties given by the 16th and 84th percentile values.

This process is run ten times to remove any bias due to the assignment of galaxy locations. In all runs, the ratio between the overdensity and field SMF shows no evidence of the increased high-mass to low-mass galaxy ratio seen in the observations. The result of an example run is shown in Figure B1. We note that this test does not include consideration of spectroscopic redshifts, which would reduce the size of uncertainties further.

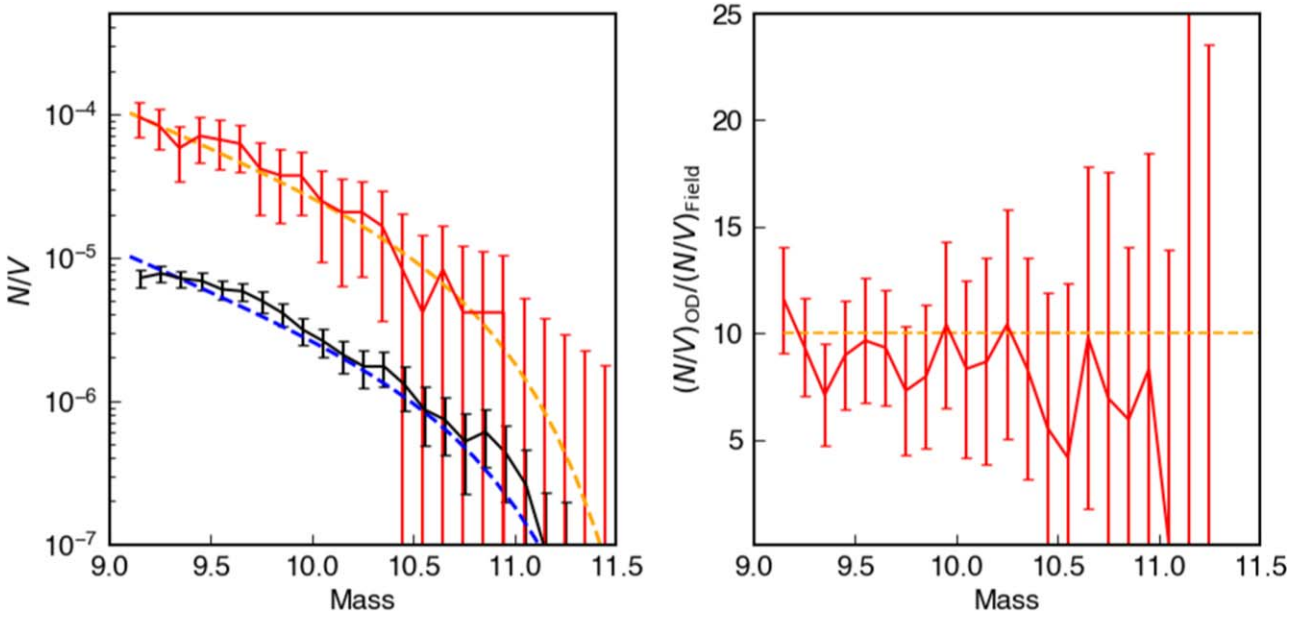

Figure B1. The result of an example run of the model to test for the effect of biases on the SMF ratios. Left: the generating SMFs for field and overdensity are shown as blue and orange-dashed curves, respectively, and the recovered SMFs are plotted as red and black lines. Right: the ratio of the generating SMFs (orange-dashed line) and recovered SMFs (red line). No bias toward higher SMF ratios at higher masses is observed.

ORCID iDs

Ben Forrest https://orcid.org/0000-0001-6003-0541
Brian C. Lemaux https://orcid.org/0000-0002-1428-7036
Ekta A. Shah https://orcid.org/0000-0001-7811-9042
Priti Staab https://orcid.org/0000-0002-8877-4320
Roy R. Gal https://orcid.org/0000-0001-8255-6560
Lori M. Lubin https://orcid.org/0000-0003-2119-8151
M. C. Cooper https://orcid.org/0000-0003-1371-6019
Olga Cucciati https://orcid.org/0000-0002-9336-7551
Denise Hung https://orcid.org/0000-0001-7523-140X
Ian McConachie https://orcid.org/0000-0002-2446-8770
Adam Muzzin https://orcid.org/0000-0002-9330-9108
Gillian Wilson https://orcid.org/0000-0002-6572-7089
Sandro Bardelli https://orcid.org/0000-0002-8900-0298
Letizia P. Cassarà https://orcid.org/0000-0001-5760-089X
Wenjun Chang https://orcid.org/0000-0003-2144-2943
Finn Giddings https://orcid.org/0009-0003-2158-1246
Emmet Golden-Marx https://orcid.org/0000-0001-5160-6713
Nimish Hathi https://orcid.org/0000-0001-6145-5090
Stephanie M. Urbano Stawinski https://orcid.org/0000-0001-8169-7249
Elena Zucca https://orcid.org/0000-0002-5845-8132

References

Ahad, S. L., Muzzin, A., Bahé, Y. M., & Hoekstra, H. 2024, MNRAS, 528, 6329
Aihara, H., Alsayyad, Y., Ando, M., et al. 2019, PASJ, 71, 1
Alberts, S., Adams, J., Gregg, B., et al. 2022, ApJ, 927, 235
Annunziatella, M., Biviano, A., Mercurio, A., et al. 2014, A&A, 571, A80
Annunziatella, M., Mercurio, A., Biviano, A., et al. 2016, A&A, 585, A160
Arnouts, S., Cristiani, S., Moscardini, L., et al. 1999, MNRAS, 310, 540
Ashby, M. L., Willner, S. P., Fazio, G. G., et al. 2013, ApJ, 769, 80
Ashby, M. L., Willner, S. P., Fazio, G. G., et al. 2015, ApJS, 218, 33
Ashby, M. L. N., Caputi, K. I., Cowley, W., et al. 2018, ApJS, 237, 39
Bahé, Y. M., Barnes, D. J., Vecchia, C. D., et al. 2017, MNRAS, 470, 4186
Bahé, Y. M., Schaye, J., Barnes, D. J., et al. 2019, MNRAS, 485, 2287
Balogh, M. L., Gilbank, D. G., Muzzin, A., et al. 2017, MNRAS, 470, 4168
Balogh, M. L., Navarro, J. F., & Morris, S. L. 2000, ApJ, 540, 113
Balogh, M. L., van der Burg, R. F. J., Muzzin, A., et al. 2020, MNRAS, 31, 358
Baxter, D. C., Cooper, M. C., Balogh, M. L., et al. 2022, MNRAS, 515, 5479
Blanton, M. R., & Moustakas, J. 2009, ARA&A, 47, 159
Bruzual, G., & Charlot, S. 2003, MNRAS, 344, 1000
Bundy, K., Ellis, R. S., Conselice, C. J., et al. 2006, ApJ, 651, 120
Calzetti, D., Armus, L., Bohlin, R. C., et al. 2000, ApJ, 533, 682
Capak, P. L., Riechers, D., Scoville, N. Z., et al. 2011, Natur, 470, 233
Casey, C. M., Cooray, A., Capak, P., et al. 2015, ApJL, 808, L33
Cassata, P., Tasca, L. A., Le Fèvre, O., et al. 2015, A&A, 573, A24
Chabrier, G. 2003, PASP, 115, 763
Chartab, N., Mobasher, B., Darvish, B., et al. 2020, ApJ, 890, 7
Chiang, Y.-K., Overzier, R. A., Gebhardt, K., & Henriques, B. 2017, ApJL, 844, L23
Cooper, M. C., Coil, A. L., Gerke, B. F., et al. 2010a, MNRAS, 409, 337
Cooper, M. C., Gallazzi, A., Newman, J. A., & Yan, R. 2010b, MNRAS, 402, 1942
Cooper, M. C., Newman, J. A., Davis, M., Finkbeiner, D. P., & Gerke, B. F., 2012 spec2d: DEEP2 DEIMOS Spectral Pipeline, Astrophysics Source Code Library, ascl:1203.003
Cucciati, O., Lemaux, B. C., Zamorani, G., et al. 2018, A&A, 619, A49
Cucciati, O., Zamorani, G., Lemaux, B. C., et al. 2014, A&A, 570, A16
Daddi, E., Dickinson, M., Morrison, G., et al. 2007, ApJ, 670, 156
Davidzon, I., Ilbert, O., Laigle, C., et al. 2017, A&A, 605, A70
De Lucia, G., Fontanot, F., Xie, L., & Hirschmann, M. 2024, A&A, 687, A68
De Lucia, G., Weinmann, S., Poggianti, B. M., Aragón-Salamanca, A., & Zaritsky, D. 2012, MNRAS, 423, 1277
Donnari, M., Pillepich, A., Joshi, G. D., et al. 2020, MNRAS, 500, 4004
Donnari, M., Pillepich, A., Nelson, D., et al. 2021, MNRAS, 506, 4760
Dressler, A. 1984, ApJ, 281, 512
Edward, A. H., Balogh, M. L., Bahé, Y. M., et al. 2023, MNRAS, 527, 8598
Faber, S. M., Phillips, A. C., Kibrick, R. I., et al. 2003, Proc. SPIE, 4841, 1657
Fitzpatrick, E. L., & Massa, D. 1986, ApJ, 307, 286
Forrest, B., Lemaux, B. C., Shah, E., et al. 2023, MNRAS, 526, L56
Forrest, B., Marsan, Z. C., Annunziatella, M., et al. 2020, ApJ, 903, 47
Forrest, B., Tran, K.-V. H., Broussard, A., et al. 2017, ApJL, 838, L12
Fujita, Y. 2004, PASJ, 56, 29
Fumagalli, M., Krumholz, M. R., Prochaska, J. X., Gavazzi, G., & Boselli, A. 2009, ApJ, 697, 1811
Hasinger, G., Capak, P., Salvato, M., et al. 2018, ApJ, 858, 77
Hatch, N. A., Kurk, J. D., Pentericci, L., et al. 2011, MNRAS, 415, 2993
Horne, K. 1986, PASP, 98, 609
Hung, D., Lemaux, B. C., Gal, R. R., et al. 2020, MNRAS, 491, 5524
Hunter, J. D. 2007, CSE, 9, 90
Hutchison, T., Walawender, J., & Kwok, S. 2020, Proc. SPIE, 11447, 114476A
Ilbert, O., Arnouts, S., McCracken, H. J., et al. 2006, A&A, 457, 841
Ilbert, O., Capak, P., Salvato, M., et al. 2009, ApJ, 690, 1236
Ilbert, O., McCracken, H. J., Le Fèvre, O., et al. 2013, A&A, 556, A55
Ito, K., Tanaka, M., Valentino, F., et al. 2023, ApJL, 945, L9
Jin, S., Dannerbauer, H., Emonts, B., et al. 2021, A&A, 652, A11
Kauffmann, G., White, S. D., Heckman, T. M., et al. 2004, MNRAS, 353, 713
Kawinwanichakij, L., Papovich, C., Quadri, R. F., et al. 2017, ApJ, 847, 134
Koekemoer, A. M., Aussel, H., Calzetti, D., et al. 2007, ApJS, 172, 196
Kriek, M., Shapley, A. E., Reddy, N. A., et al. 2015, ApJS, 218, 1
Kukstas, E., Balogh, M. L., Mccarthy, I. G., et al. 2023, MNRAS, 518, 4782
Laigle, C., McCracken, H. J., Ilbert, O., et al. 2016, ApJS, 224, 24
Le Fèvre, O., Cassata, P., Cucciati, O., et al. 2013, A&A, 559, A14
Le Fèvre, O., Saisse, M., Mancini, D., et al. 2003, Proc. SPIE, 4841, 1670
Le Fèvre, O., Tasca, L. A. M., Cassata, P., et al. 2015, A&A, 576, A79
Le Fèvre, O., Vettolani, G., Paltani, S., et al. 2004, A&A, 428, 1043
Leauthaud, A., Massey, R., Kneib, J., et al. 2007, ApJS, 172, 219
Leja, J., Johnson, B. D., Conroy, C., et al. 2019, ApJ, 877, 140
Lemaux, B. C., Cucciati, O., Le Fèvre, O., et al. 2022, A&A, 662, A33
Lemaux, B. C., Cucciati, O., Tasca, L. A., et al. 2014, A&A, 572, A41
Lemaux, B. C., Le Fèvre, O., Cucciati, O., et al. 2018, A&A, 615, A77
Lemaux, B. C., Lubin, L. M., Sawicki, M., et al. 2009, ApJ, 700, 20
Lemaux, B. C., Tomczak, A. R., Lubin, L. M., et al. 2017, MNRAS, 472, 419
Lemaux, B. C., Tomczak, A. R., Lubin, L. M., et al. 2019, MNRAS, 490, 1231
Lilly, S. J., Fevre, O. L., Renzini, A., et al. 2007, ApJS, 172, 70
Lubin, L. M., Gal, R. R., Lemaux, B. C., Kocevski, D. D., & Squires, G. K. 2009, AJ, 137, 4867
Marchesini, D., Van Dokkum, P. G., Förster Schreiber, N. M., et al. 2009, AJ, 701, 1765
Marsan, Z. C., Muzzin, A., Marchesini, D., et al. 2022, ApJ, 924, 25
McConachie, I., Wilson, G., Forrest, B., et al. 2022, ApJ, 926, 37
McCracken, H. J., Milvang-Jensen, B., Dunlop, J., et al. 2012, A&A, 544, A156
McGee, S. L., Balogh, M. L., Bower, R. G., Font, A. S., & McCarthy, I. G. 2009, MNRAS, 400, 937
McLean, I. S., Steidel, C. C., Epps, H., et al. 2010, Proc. SPIE, 7735, 77351E
McLean, I. S., Steidel, C. C., Epps, H. W., et al. 2012, Proc. SPIE, 8446, 84460J
Mei, S., Hatch, N. A., Amodeo, S., et al. 2023, A&A, 670, A58
Mobasher, B., Dahlen, T., Ferguson, H. C., et al. 2015, ApJ, 808, 101
Moneti, A., Mccracken, H. J., Hudelot, P., et al. 2019, ESO Science Archive Facility - Phase 3 Data Release Description, http://ultravista.org/release4/
Muldrew, S. I., Hatch, N. A., & Cooke, E. A. 2015, MNRAS, 452, 2528
Muzzin, A., Marchesini, D., Stefanon, M., et al. 2013a, ApJS, 206, 8
Muzzin, A., Marchesini, D., Stefanon, M., et al. 2013b, ApJ, 777, 18
Muzzin, A., Wilson, G., Yee, H. K. C., et al. 2012, ApJ, 746, 188
Nantais, J. B., van der Burg, R. F. J., Lidman, C., et al. 2016, A&A, 592, A161
Newman, J. A., Cooper, M. C., Davis, M., et al. 2013, ApJS, 208, 5
Noble, A. G., Muzzin, A., McDonald, M., et al. 2019, ApJ, 870, 56
Noeske, K. G., Weiner, B. J., Faber, S. M., et al. 2007, ApJL, 660, L43
Oke, J. B., & Gunn, J. E. 1983, ApJ, 266, 713
Oliphant, T., & Millma, J. k. 2007, CSE, 9, 10
Onodera, M., Renzini, A., Carollo, M., et al. 2012, ApJ, 755, 26
Papovich, C., Kawinwanichakij, L., Quadri, R. F., et al. 2018, ApJ, 854, 30
Peng, Y.-j., Lilly, S. J., Kovač, K., et al. 2010, ApJ, 721, 193
Pérez, F., & Granger, B. E. 2007, CSE, 9, 21
Pérez-Martínez, J. M., Dannerbauer, H., Kodama, T., et al. 2022, MNRAS, 518, 1707
Pérez-Martínez, J. M., Kodama, T., Koyama, Y., et al. 2023, MNRAS, 527, 10221

Pickles, A. 1998, PASP, 110, 863
Pillepich, A., Nelson, D., Hernquist, L., et al. 2018, MNRAS, 475, 648
Polletta, M., Tajer, M., Maraschi, L., et al. 2007, ApJ, 663, 81
Prevot, M. L., Lequeux, J., Prevot, L., Maurice, E., & Rocca-Volmerange, B. 1984, A&A, 132, 389
Price-Whelan, A. M., Sipőcz, B. M., Günther, H. M., et al. 2018, AJ, 156, 123
Reeves, A. M., Balogh, M. L., Van Der Burg, R. F., et al. 2021, MNRAS, 506, 3364
Robitaille, T. P., Tollerud, E. J., Greenfield, P., et al. 2013, A&A, 558, A33
Salmon, B., Papovich, C., Finkelstein, S. L., et al. 2015, ApJ, 799, 183
Sawicki, M., Arnouts, S., Huang, J., et al. 2019, MNRAS, 489, 5202
Schechter, P. 1976, ApJ, 203, 297
Schreiber, C., Glazebrook, K., Nanayakkara, T., et al. 2018b, A&A, 618, A85
Schreiber, C., Labbé, I., Glazebrook, K., et al. 2018a, A&A, 611, A22
Scoville, N., Aussel, H., Brusa, M., et al. 2007, ApJS, 172, 1
Shah, E. A., Kartaltepe, J. S., Magagnoli, C. T., et al. 2022, ApJ, 940, 4
Shah, E. A., Lemaux, B., Forrest, B., et al. 2024, MNRAS, 529, 873
Shen, J., Man, A. W. S., Zabl, J., et al. 2021a, ApJ, 917, 79
Shen, L., Lemaux, B. C., Lubin, L. M., et al. 2021b, ApJ, 912, 60
Sherman, S., Jogee, S., Florez, J., et al. 2020, MNRAS, 491, 3318
Shi, K., Toshikawa, J., Lee, K.-S., et al. 2021, ApJ, 911, 46
Shimakawa, R., Kodama, T., Hayashi, M., et al. 2018a, MNRAS, 473, 1977
Shimakawa, R., Koyama, Y., Röttgering, H. J., et al. 2018b, MNRAS, 481, 5630
Staab, P., Lemaux, B. C., Forrest, B., et al. 2024, MNRAS, 528, 6934
Stefanon, M., Marchesini, D., Muzzin, A., et al. 2015, ApJ, 803, 11
Steinhardt, C. L., Capak, P., Masters, D., & Speagle, J. S. 2016, ApJ, 824, 21
Steinhardt, C. L., Speagle, J. S., Capak, P., et al. 2014, ApJL, 791, L25
Straatman, C. M. S., Spitler, L. R., Quadri, R. F., et al. 2016, ApJ, 830, 51
Taamoli, S., Mobasher, B., Chartab, N., et al. 2024, ApJ, 966, 18
Taniguchi, Y., Kajisawa, M., Kobayashi, M. A., et al. 2015, PASJ, 67, 1
Taniguchi, Y., Scoville, N., Murayama, T., et al. 2007, ApJS, 172, 9
The Astropy Collaboration, Price-Whelan, A. M., Lim, P. L., et al. 2022, ApJ, 935, 167
Thomas, D., Maraston, C., Bender, R., & de Oliveira, C. M. 2005, ApJ, 621, 673
Tomczak, A. R., Lemaux, B. C., Lubin, L. M., et al. 2017, MNRAS, 472, 3512
Tomczak, A. R., Quadri, R. F., Tran, K.-v. H., et al. 2014, ApJ, 783, 85
Tran, K.-V. H., Papovich, C., Saintonge, A., et al. 2010, ApJ, 719, L126
van der Burg, R. F., Muzzin, A., Hoekstra, H., et al. 2013, A&A, 557, A15
van der Burg, R. F. J., McGee, S., Aussel, H., et al. 2018, A&A, 618, A140
van der Burg, R. F. J., Rudnick, G., Balogh, M. L., et al. 2020, A&A, 638, A112
Wang, B., Leja, J., Atek, H., et al. 2024, ApJ, 963, 74
Wang, T., Elbaz, D., Daddi, E., et al. 2016, ApJ, 828, 56
Weaver, J. R., Davidzon, I., Toft, S., et al. 2023, A&A, 677, A184
Weaver, J. R., Kauffmann, O. B., Ilbert, O., et al. 2022, ApJS, 258, 11
Webb, K., Balogh, M. L., Leja, J., et al. 2020, MNRAS, 498, 5317
Werner, S. V., Hatch, N. A., Muzzin, A., et al. 2022, MNRAS, 510, 674
Whitaker, K. E., Labbé, I., van Dokkum, P. G., et al. 2011, ApJ, 735, 86
Williams, C. C., Alberts, S., Spilker, J. S., et al. 2022, ApJ, 929, 35
Williams, R. J., Quadri, R. F., Franx, M., van Dokkum, P., & Labbé, I. 2009, ApJ, 691, 1879
Zabludoff, A. I., Zaritsky, D., Lin, H., et al. 1996, ApJ, 466, 104
Zamojski, M. A., Schiminovich, D., Rich, R. M., et al. 2007, ApJS, 172, 468
Zavala, J. A., Casey, C. M., Scoville, N., et al. 2019, ApJ, 887, 183